Title Page

Oncogene-induced senescence and senescence-associated secretory phenotype (SASP) determine the efficacy of palbociclib in PIK3CA mutated colorectal cancer

Authors and affiliations:

Pingping Cao[1,†], Xiaohui Zhou[1,†], Suisui Yang[1,†], Tianqi Shen[1], Shuai Wang[2], Hanyang Yu[1], Xiaorong Liu[1], Yeqing Gong[3], WenHong Wang[1], Haiyang Wang[4], Tingting Zhou[1], Jing Wang[1], Zhining Fan[4], Mingde Huang[5], Xu Qian[6,7], Xiuxing Wang[1,7], Qianghu Wang[7,8], Liu Yang[9]*, Yingjian Zhang[2]*, Fan Lin[1,2,5,7]

[1] Department of Cell Biology, School of Basic Medical Sciences, Nanjing Medical University Nanjing, Jiangsu, P. R. China

[2] Henan Medical Key Laboratory of Gastrointestinal Microecology and Hepatology; Department of Gastroenterology, The First Affiliated Hospital, College of Clinical Medicine, Henan University of Science and Technology, Luoyang 471003, Henan, P. R. China

[3] CAS Center for Excellence in Molecular Cell Science, Shanghai Institute of Biochemistry and Cell Biology, University of Chinese Academy of Sciences, Chinese Academy of Sciences, Shanghai 200031, P. R. China

[4] Department of Digestive Endoscopy, The First Affiliated Hospital with Nanjing Medical University, Nanjing 210029, P. R. China

[5] Department of Oncology, The Affiliated Huaian No.1 People's Hospital of Nanjing Medical University, Northern Jiangsu Institute of Clinical Medicine, Huaian 223300, P. R. China

[6] Department of Nutrition and Food Hygiene, Center for Global Health, School of Public Health, Nanjing Medical University, Nanjing 211166, P. R. China

[7] Institute for Brain Tumors, Jiangsu Collaborative Innovation Center for Cancer Personalized Medicine, Nanjing Medical University, Nanjing 211166, P. R. China

[8] Department of Bioinformatics, Nanjing Medical University, Nanjing 211166, P. R. China

[9] Nanjing Medical University Affiliated Cancer Hospital & Jiangsu Cancer Hospital & Jiangsu Institute of Cancer Research, Nanjing, Nanjing, 210009, P. R. China

P. Cao, X. Zhou and S. Yang equally contributed as a first author for this article.

L. Yang, Y. Zhang and F. Lin equally contributed as a last author for this article.

Corresponding Authors:

Liu Yang, 42# Baizting, Nanjing, Jiangsu, Nanjing, P.R. China. E-mail:yangliu@njmu.edu.cn

Yingjian Zhang, No. 24 Jinghua Road, Jianxi District, Luoyang, Henan, P.R. China.

Email: Yingzhangyingjian@haust.edu.cn

Fan Lin (primary contact), XueHai Building A111, Nanjing Medical University, 101 Longmian Avenue, Jiangning District, Nanjing, P.R. China. E-mail: linfee@me.com

Words of abstract: 146

Words of text: 5928

Number of figures: 7

Number of Supplemental documents: 2

Number of references: 41

ABSTRACT

Palbociclib is an excellent CDK4/6 inhibitor, but its clinical application is mainly limited to the treatment of advanced ER^+/HR^+ and $HER2^-$ breast cancer. Its efficacy in colorectal cancer (CRC) is evaluated in multiple trials and so far remains undetermined. We found that the PIK3CA-mutant CRC cells were insensitive to palbociclib treatment compared with the PIK3CA wild-type counterparts, and they were in an OIS (oncogene-induced senescence) state which was predisposed to a strong senescence-associated secretory phenotype (SASP) upon treatment. These senescent cells excessively secreted various SASP factors LCN2, and ultimately caused palbociclib-resistance via upregulation of EGFR in the non-senescent CRC cells. Importantly, a drug combination screen identified that erlotinib could synergize with palbociclib to overcome the SASP-induced resistance. Overall, we found that PIK3CA mutation-induced senescence compromised the efficacy of palbociclib treatment in CRC but co-targeting EGFR could minimize the OIS-associated side effects while preserving the beneficial effects.

SIGNIFICANCE: Oncogene-induced senescence is commonly known as an antitumor defense mechanism. Here we discovered it could also act as an accomplice of CRC cells in CDK4/6-targeted therapy and jeopardize its clinical application. However, concurrent treatment with EGFR and CDK4/6 inhibitors can overcome the OIS-associated side effects and achieve significant anti-CRC efficacy.

INTRODUCTION

Colorectal cancer (CRC) is a global leading cause of cancer-related morbidity and mortality in both men and women (1). Currently, radio- and chemo-therapy are still the mainstays for post-surgical treatment of CRC, and are often accompanied by severe side effects, limited efficacy, easy recurrence and metastasis (2). Palbociclib (Ibrance™, Pfizer) is the first CDK4/6 inhibitor that has been approved by the FDA in 2015 for the first-line treatment of postmenopausal women with HR/ER-positive and HER2-negative advanced breast cancer in combination with letrozole (3). Due to its good clinical efficacy in breast cancer, several clinical trials involving the use of CDK4/6 inhibitors alone or in combination with chemotherapeutic/targeted agents have been tried in the treatment of CRC (https://clinicaltrials.gov). Although some improvement and efficacy have been observed, a decisive conclusion about the usefulness of palbociclib in the treatment of CRC is yet to be made, and further investigations are still required (4,5).

Abnormal cell proliferation caused by dysregulation of the cell cycle is one of the hallmark characteristics of tumors (6). Normally, gradual accumulation of cyclin in the G1 phase activates CDK4 and/or CDK6, two Cyclin-dependent kinases, leading to phosphorylation of the RB and activation of E2F transcription of downstream genes required by cell cycle progression (7). Whereas, CDK4/6 are often overexpressed or continuously being activated in various tumors including CRC cells, so their cell cycle is often shortened and the proliferation is accelerated (8). Palbociclib or several other CDK4/6 targeted inhibitors exert their activities by competitively binding to the ATP-binding pocket of CDK4/6 to inactivate the CDK4/6-Cyclin D complexes, leading to inhibition of RB phosphorylation and subsequent blockage of the cell cycle.

Besides the cell cycle arrest, another therapeutic effect caused by palbociclib is the induction of senescence (9-11). Cellular senescence is a state of terminal growth arrest in which cells are unresponsive to growth factor stimulation, and it could be induced by telomere shortening, intracellular ROS accumulation, oncogene activation, chemo- or radiotherapy, and cell cycle targeted therapy in our case (12-15). According to previous studies, senescent cells permanently lose their ability to re-enter the cell cycle and proliferate, so both oncogene-induced senescence (OIS) and therapy-induced senescence (TIS) are always regarded as a protective mechanism or treatment-favorable roles for preventing the tumor genesis and development (16).

However, in this study, we found a novel phenomenon that the OIS caused by the gain-of-function mutation of PIK3CA may not act as a protective barrier but as an accomplice of palbociclib resistance and tumor progression in CRC cells. In these cells, we not only observed strong expression of senescence markers which was putatively driven by OIS, but also found that the senescence phenotype was further aggravated by palbociclib treatment. Unfortunately, the additive effect of palbociclib-induced TIS and PIK3CA-mutation-induced OIS was found to prominently counteract the efficacy of palbociclib, but not the opposite.

Senescent cells can have pleiotropic functions in cancer, aging, and other disease. This is due to their ability to secrete an array of inflammatory cytokines, chemokines, and matrix proteases (the senescence-associated secretory phenotype, SASP), and cause beneficial or detrimental effects on the tumor or its microenvironment in a context-dependent manner (17,18). In the present study, we discovered that the SASP factor(s) secreted by the PIK3CA mutant CRC cells conferred resistance to palbociclib via upregulation of EGFR in the adjacent non-senescent cells, and it could be overcome by

combining palbociclib with an EGFR inhibitor. In this way, we proposed a new senotherapy that only targets the major effector molecule in the affected cells instead of trying to eliminate all the senescent cells in the senolytic therapy or suppress the senescence and SASP in the senomorphic therapy, so the beneficial side of palbociclib-induced senescence could still be preserved. Furthermore, our study delivers a promising therapeutic approach utilizing a combination of two FDA-approved drugs for the treatment of PIK3CA mutant CRC that currently lacks targeted therapeutic approaches.

RESULTS

1. Gain-of-function mutations of the PIK3CA gene confer resistance to palbociclib in colorectal cancer cells.

Firstly, we assessed the anticancer efficacy of palbociclib in CRC cell lines and accidentally found a tendency that those carrying gain-of-function mutation of the PIK3CA gene were more resistant to palbociclib treatment by both anti-proliferation (Fig. 1A) and clonogenic assays (Fig. 1B). The average IC50 of three PIK3CA mutant CRC cell lines, namely, HCT116, HCT15, and DLD1 were approximately 2-fold higher than that of LOVO and SW620, two CRC cell lines carrying wild-type PIK3CA (Fig. 1A and C), while the genetic status of TP53 did not seem to be related to the palbociclib sensitivity (Fig. S1A). In addition, the clinically relevant concentration of palbociclib (up to 500 ng/mL ≈ 1.12 μM) (19) failed to cause sufficient apoptosis in PIK3CA mutant cell lines (Fig. S1B and C). Interestingly, this is not due to the insufficient inhibition of the targeted protein or arrest of the cell cycle by palbociclib treatment, as the level of p-RB and FoxM1 were markedly declined from 0.5 μM related to control (Fig. 1D), and substantial cells were detained in G1 phase even at a very low concentration of 0.1 μM in PIK3CA mutant cell lines (Fig. S1D and E). By a joint analysis of the drug sensitivity data from GDSC (https://www.cancerrxgene.org/) and mutation data of CRC cell lines from COSMIC (http://cancer.sanger.ac.uk), only TP53 and PIK3CA exhibited much higher mutation frequency in palbociclib resistant (27 cell lines) than sensitive (14 cell lines) CRC cell lines in the top 10 most frequently mutated genes in all CRC cell lines (Fig. 1E). Moreover, PIK3CA is the 5th most frequently mutated gene in 386 clinical CRC samples and the missense mutations of E545K/G and H1047R/L are two predominant forms of its mutation which were also occurred in HCT116 (H1047R/G), HCT15 and DLD1 (E545K/L) cell lines (Fig. 1F).

If the therapeutic effect of palbociclib in the treatment of CRC is indeed determined by the genetic

status of the PIK3CA gene, the clinical efficacy of CDK4/6 targeted therapy could be compromised in about 1/3 of all CRC patients. To confirm this finding, we constructed PIK3CA wild-type (WT) and mutant (MUT) isogeneic cell lines using LOVO cells that originally carried the WT PIK3CA gene. The levels of phosphorylated AKT of MUT E545K (2# and 5#) and H1047R (2# and 3#) cell lines were much higher than the WT counterparts, confirming their PI3K-AKT signaling being continuously activated (Fig. S1F). Moreover, LOVO cells carrying either PIK3CA E545K or H1047R mutations were more insensitive to palbociclib than the WT counterparts in the anti-proliferation (Fig. S1G) and colony formation assay (Fig. S1H).

To further validate this PIK3CA-associated resistance phenotype *in vivo*, we established a xenograft model by subcutaneously injecting the aforementioned WT, E545K (2#), and H1047R (3#) LOVO cells to immunodeficient NNG mice to evaluate the efficacy of palbociclib. As shown in Fig. 1G-I, oral administration of 25 mg/kg palbociclib caused significant tumor suppression and prolonged overall survival in mice carrying WT PIK3CA. The H&E and Ki-67 immunohistochemical staining also confirmed that the palbociclib treatment caused clear tumor growth inhibition and regression (more necrotic region and less Ki-67 positive cells) relative to those from the control group in which mice received only vehicle solution (Fig. S1I). In contrast, palbociclib only marginally suppressed the growth of PIK3CA E545K and H1047R tumors and failed to cause a statistically meaningful improvement in the survival of mice in these groups compared with the control group. The H&E and Ki-67 staining of tumor tissue also reflected a similar trend (Fig. 1G-I and Fig S1I). Lastly, we did not observe marked body weight loss or any other severe side effects during the three weeks of treatment (Fig. S1J). Together, the above results suggest that patients harboring PIK3CA E545K and H1047R mutated CRC tumors could not benefit from the palbociclib treatment despite that it was a safe and efficacious therapy for PIK3CA WT tumor formed by LOVO cells.

2. Palbociclib treatment aggravated the PIK3CA mutation-induced senescence and senescence-associated secretory phenotype.

To interrogate the molecular mechanism that PIK3CA mutation conferred resistance to palbociclib, we performed RNA-seq for PIK3CA WT and PIK3CA MUT LOVO cells treated with palbociclib or vehicle solution (Fig. 2A). KEGG pathway analysis revealed that Cellular Senescence was the top 6 enriched pathways in PIK3CA WT cells (Fig. 2B), and it was even more enriched and ranked the top 3

among all enriched pathways in PIK3CA MUT cells upon palbociclib treatment (Fig. 2C). To confirm the bioinformatic analysis-derived outcome, we performed β-galactosidase staining and Western blotting to determine several senescence biomarkers in CRC cells. As a result, CRC cells carrying PIK3CA E545K or H1047R mutation were not only more apt to the SA-β-galactosidase (β-GAL) positive senescent phenotype (Fig. 2D and E) but also exhibited higher levels of p21 than the WT cells after palbociclib treatment (Fig. 2F). In addition, the p21 level was also upregulated in HCT116 and HCT15 cell lines carrying intrinsic PIK3CA mutation by palbociclib treatment in a dose-dependent manner (Fig. S2A and B). Interestingly, the expressions of p21, p27, and p53 were higher in PIK3CA MUT cells than in WT cells even without treatment (Fig. 2G), but the cell cycle-related proteins in the G1 phase remained unaltered (Fig. 2H). Together, these results suggested that the PIK3CA MUT cells had a higher basal level of senescence than WT cells due to oncogene-induced senescence, and this senescence phenotype was further aggravated by the palbociclib-induced senescence.

Next, GSEA was performed and revealed that palbociclib treatment resulted in significant enrichment of the Inflammatory Responses and Lysosomes pathways genes (p = 0.017 and p = 5.27E-04, respectively) in PI3KCA MUT cells but not in WT cells (Fig. 2I). Since both lysosomal dysfunction and aberrant local inflammation were features of cellular senescence (20-22), we postulated that the upregulation of inflammatory response pathways in palbociclib-treated PIK3CA MUT cells may be related to the alteration of cytokine/chemokine-factors secreted due to the senescence-associated secretory phenotype (SASP) (23). Indeed, palbociclib treatment generated 496 and 231 exclusive differentiated expressed genes (DEGs) of SASP factors (SASPF) in PIK3CA WT and MUT cells, respectively, and 240 common SASPF-DEGs in both PIK3CA WT and MUT cells (Fig. 2J Venn diagram). Heatmap analysis of the 240 common SASPF-DEGs revealed that the expression patterns of the vehicle-treated PIK3CA WT and MUT cells were similar, whereas those of palbociclib-treated PIK3CA MUT cells were quite different from the PIK3CA WT cells (Fig. 2J Heatmap). Moreover, 49 and 85 SASPF genes were significantly downregulated and upregulated ($\log_2$FC >1.5) in PIK3CA MUT cells, respectively, but only approximately half of the SASPF-DEGs were significantly altered in PIK3CA WT cells treated with palbociclib (Fig. 2K). The above evidence indicated that the pronounced alteration of transcription of SASPF genes occurred in PIK3CA MUT cells post-treatment. To confirm it, several representative SASPF were selected and their expression in PIK3CA WT and MUT cells post-treatment was assessed by q-PCR. As shown in Fig. 2L and Fig. S2 C

and D, palbociclib treatment significantly elevated the expression of IL6, CCL2, MMP1, and CXCL8 in PIK3CA MUT but not in WT LOVO cells, and this phenomenon was also observed in the CRC cell lines carrying intrinsic PIK3CA mutation.

3. SASP factors secreted from palbociclib-treated PIK3CA mutant cells caused resistance to palbociclib and elevation of EGFR

We wondered whether the altered expression of SASPF genes in palbociclib-treated PIK3CA MUT cells could be the cause of palbociclib resistance, so a series of experiments were designed to evaluate the effect of the condition medium collected from vehicle-treated PIK3CA WT/MUT LOVO cells (Control CM) or palbociclib-induced senescent PIK3CA WT/MUT cells (S-CM, Fig. 3A). Compared with the post-treatment S-CM derived from PIK3CA WT cells, the PIK3CA MUT cells derived S-CM was capable of accelerating the short-term proliferation (Fig. 3B), long-term colony formation (Fig. 3C), and conferring resistance to palbociclib in the same type of cells cultured with S-CM (Fig. 3D).

To determine which pathways might be involved in the S-CM-induced palbociclib resistance, KEGG and GSEA analyses of the RNA-seq data from Control CM *vs* S-CM-treated PIK3CA MUT cells were performed. Interestingly, both PI3K-AKT/mTOR and MAPK/MEK signaling pathways were significantly enriched by GSEA or KEGG analyses (Fig. 3E and Fig. S3A). Moreover, the ERBB family-related gene sets were also significantly enriched (Fig. 3E). Therefore, we inferred that the aberrant EGFR and its downstream signaling could be the cause of palbociclib resistance. To confirm this finding, S-CM was collected and used for the treatment of PIK3CA WT/MUT LOVO cells for different time durations or with different mixing ratios with DMEM (complete medium). Although the S-CM caused elevations of EGFR, p-EGFR, and its downstream molecules in both PIK3CA WT and MUT cells over time, the elevations were more prominent in the PIK3CA MUT cell lines. Meanwhile, increasing the mixing ratio of S-CM/DMEM also caused elevation of EGFR and p-EGFR in PIK3CA MUT cells but not in WT cells (Fig. 3F). We also confirmed that the upregulation of EGFR was due to the extracellular signal but not due to the intracellular regulation because the basal level of EGFR was not different between the PIK3CA WT and MUT cell lines (cultured for 24 hr, Fig. 3G). Moreover, immunohistochemical staining of EGFR of the PIK3CA WT/MUT tumor tissue from the xenograft mice received vehicle or 25 mg/kg of palbociclib (p.o.) again showed that the EGFR expression in

PIK3CA MUT tumors was markedly increased by palbociclib treatment, but such increase was not observed in PIK3CA WT tumors (Fig. S3F and G).

The next question was whether the elevated EGFR level responsible for the palbociclib resistance. To study that, we established EGFR overexpressed (OE-EGFR) LOVO and SW620 cells (Fig. 3H) and harvested the cell pellets from parental LOVO and OE-EGFR cells for data-independent acquisition mass spectrometry analysis (DIA-MS). Overexpression of EGFR markedly increased the tolerance of LOVO and SW620 cells to palbociclib treatment in the anti-proliferation (Fig. 3I) and colony formation (Fig. 3J) experiments. Mechanism study using GO analysis of the proteomic data discovered that the EGFR overexpression resulted in significant enrichment in cell division, cell cycle, G2/M transition, and mitosis-related pathways (Fig. S3C). In addition, GSEA revealed the enrichment of cell cycle-related genes in both S-CM treated PIK3CA MUT (Fig. S3B) and OE-EGFR LOVO cells (Fig. S3D), suggesting a similar consequence being caused by S-CM treatment or EGFR overexpression. The Heatmap exhibited that the expression pattern of 84 cell cycle-related genes of OE-EGFR cells was markedly different from the parental LOVO cells (Fig. S3E). Importantly, some of the significantly altered cell cycle genes in the OE-EGFR cells, such as CDK2, RB1, MDM2, WEE1, etc. were previously reported to cause palbociclib resistance. To obtain a comprehensive profile of EGFR-induced palbociclib resistance, we established a palbociclib resistance-related geneset by combining the patient's data-derived palbociclib resistant genes and literature-based palbociclib resistance genes (Fig. S3H and Supplemental Table 1) (24). As shown in Fig. S3I, the GSEA enrichment plots revealed that the above palbociclib resistance genes were significantly enriched in both S-CM-treated PIK3CA MUT and OE-EGFR LOVO cells. Finally, WB confirmed several representative proteins that were involved in palbociclib resistance (Fig. S3J) and cell cycle in OE-EGFR LOVO cells (Fig. S3K). The above results suggested that instead of alteration of a certain protein, both S-CM treatment and EGFR overexpression caused extensive changes of various proteins which cooperatively boosted the palbociclib resistance in recipient CRC cells.

4. SASP factor LCN2-mediated EGFR upregulation was essential for palbociclib resistance

To identify the factor that contributes to the elevation of EGFR in the S-CM derived from PIK3CA-mutated senescent cells, we analyzed the SASPF genes that were significantly upregulated (> 2-fold) in the palbociclib-treated PIK3CA MUT cells. Consequently, 16 SASPF genes exhibited higher

expression in PIK3CA MUT than WT cells from 32 SASPF genes that were commonly upregulated in both PIK3CA WT and MUT cells, and 53 from a total of 85 significantly upregulated SASPF genes that were exclusively present in the palbociclib-treated PIK3CA MUT but not WT cells were selected (Fig. S4A). The differentiated gene expression pattern of the total 69 selected SASPF genes in vehicle/palbociclib-treated PIK3CA MUT cells was illustrated in a heatmap in Fig. 4A.

Next, we analyzed the potential interactions between 69 SASPF and EGFR using the STRING database and discovered that 23 SASP factors have interactions with EGFR (Fig. S4B). Among the 23 potential candidates, 12 SASP factors have strong interactions (combined-score >0.7, Fig. S4C) with EGFR. One of them is LCN2, a gene encoding lipocalin-2 and being reported to interact with EGFR to facilitate its recycling under TGF-α stimulation (25). By q-PCR and ELISA assays, we found that both the expression and secretion of LCN2 exhibited marked elevation upon palbociclib treatment in the PIK3CA MUT cells, but remained unaltered in PIK3CA WT cells (Fig. 4B and C). Importantly, overexpression of LCN2 in LOVO and SW620 cells caused elevation of EGFR in the protein level (Fig. 4D and E), but not in the mRNA level in both CRC cell lines (Fig. 4F and G). Moreover, correlation analyses of the multi-omics data of CRC cell lines from CCLE revealed a strong positive correlation between the protein levels of EGFR and LCN2 ($R = 0.57$, $P = 0.02$), and a relatively weak positive correlation between the mRNA levels of EGFR and LCN2 ($R = 0.29$, $P = 0.03$, Fig. S4D). Lastly, colonies formed by LCN2 overexpressed LOVO and SW620 were more resistant to palbociclib treatment than their parental cells (Fig. 4H and I). This evidence together indicates that LCN2 is the determinant SASP factor that confers resistance to palbociclib in palbociclib-treated PIK3CA MUT CRC cells.

Based on the results in Fig. 4D-G and S4D, we inferred that LCN2 may regulate EGFR via the protein-protein interaction. To confirm it, LOVO and SW620 cells overexpressing exogenous LCN2 and EGFR were co-stained with antibodies against EGFR (red) and LCN2 (green), and the fluorescence staining was visualized by confocal microscopy. As shown in Fig. 4J and K, significant colocalization of EGFR and LCN2 were observed and the two types of immunofluorescent signals were highly overlapped. Furthermore, EGFR-Flag co-immunoprecipitated with LCN2 and LCN2-Flag co-immunoprecipitated with EGFR in HEK293T cells transiently co-transfected with LCN2 (LCN2-Flag) and EGFR (EGFR-Flag), confirming the direct interaction between EGFR and LCN2 (Fig. 4L). Moreover, we also detected the interaction of endogenous EGFR and LCN2 in WT LOVO

cells, and the LCN2 co-immunoprecipitated with more EGFR in the S-CM treated PIK3CA MUT LOVO cells than the untreated control cells (Fig. S4E).

To explore how LCN2 influenced the expression of EGFR, we first inhibited the protein synthesis using cycloheximide (CHX) in CRC cells and checked their protein change of EGFR in 8 hr. The results indicated that overexpression of LCN2 significantly reduced the degradation of EGFR protein in LOVO and SW620 cells (Fig. 4M and N). In contrast, inhibition of overall RNA synthesis by actinomycin D (Act D) for 24 hr failed to prevent the degradation of EGFR in LCN2 overexpressing LOVO cells so the EGFR-protective role of LCN2 may be unrelated to transcription of EGFR (Fig. S4F). To unravel the role of LCN2 in the protection of EGFR from degradation, LOVO cells were treated with MG132, a proteasomal inhibitor, or leupeptin (Leu), a lysosomal inhibitor, in the presence/absence of CHX. The results demonstrated that both 5 and 10 μg/mL MG132 failed to protect the EGFR from degradation (Fig. 4O), but 20 μg/mL leupeptin completely abolished the EGFR degradation in the presence of CHX in LCN2 overexpressed LOVO cells and (Fig. 4P), indicating that LCN2 protects the degradation of EGFR primarily via the lysosomal degradation pathway. Since ubiquitination is known to regulate protein trafficking in the endosomal system and to target the cargo proteins for lysosomal degradation (26), we also investigated the ubiquitination of the EGFR protein in the LCN2 overexpressed and control 293T cells. As shown in Fig. 4Q, overexpression of LCN2 significantly reduces the ubiquitination levels of the EGFR protein, suggesting that it prevents EGFR from being ubiquitinated.

Previous studies suggested that LCN2 was required for TGF-α-induced EGFR recycling to the plasma membrane and its sustained activation(25). We found that the TGF-α expression (determined by q-PCR) and secretion (determined by ELISA) were significantly upregulated in both PIK3CA WT and MUT cells upon palbociclib treatment (Fig. 4R and S), so the excess stimulation of TGF-α signaling further promoted the LCN2-mediated EGFR upregulation. In addition, overexpression of LCN2 significantly increases the membrane localization of EGFR, indicating that LCN2 not only suppresses the degradation of EGFR protein but also enhances its intracellular recycling (Fig. 4T).

5. Identification of erlotinib as a palbociclib-synergizer to overcome the palbociclib resistance in PIK3CA mutant CRC cells

To overcome the palbociclib resistance, we took advantage of a previously established drug

screening workflow for rapid identification of drug-drug synergism in our lab to find effective combined therapy to treat PIK3CA mutant CRC (27) (Fig. 5A). In brief, the anti-proliferative activity of 133 clinically relevant small molecule targeted inhibitors and their combined effect with palbociclib in DLD1 were assessed, and the Sensitivity Index (SI) of each agent was calculated. As shown in Fig. 5B, the SI value of 17 agents was above 0, suggesting their potential to reverse the resistance of palbociclib and synergize its anti-CRC activity (Fig. 5B).

Among them, the highest value was achieved by erlotinib, a selective EGFR inhibitor. This finding again underscored the importance of EGFR in palbociclib resistance. To confirm the synergistic interaction between palbociclib and erlotinib in the treatment of PIK3CA MUT CRC cells, we applied the classical HSA synergy model and Chou-Talalay method to determine the high single agent (HSA) and combination index (CI) values as readouts for synergistic inhibition. The analyses were performed in both DLD1 and HCT15 cells carrying natural PIK3CA mutation and the LOVO cells carrying artificial PIK3CA E545K or H1047R mutation. As a result, most of the HSA values >0 in the concentration combination matrices (Fig. 5C and Fig. S5A) and CI values <1 in the Fa-CI plot in treatment (Fig. 5D and S5B), indicating synergistic interactions occurred in most of the palbociclib-erlotinib combinations at different concentrations. Meanwhile, *in vitro* evaluation of the anti-CRC effect of the palbociclib-erlotinib combination demonstrated that erlotinib sensitized the originally refractory DLD1 and HCT15 cells and PIK3CA MUT LOVO cells to palbociclib treatment and resulted into significant suppression of their proliferation (Fig. 5E and Fig. S5C) and colony formation (Fig. 5F and Fig. S5D) relative to the vehicle or palbociclib treatment.

To reveal the mechanism behind the palbociclib-erlotinib synergy, we analyzed the relevant signaling pathway and transcriptome alteration in PIK3CA mutant cells upon palbociclib and/or erlotinib treatment. Western blotting results demonstrated that erlotinib further aggravated the RB and p-RB inhibition by palbociclib in DLD1 and HCT15 cells. Moreover, several downstream targets of EGFR and CDK4/6 such as FOXM1, p-AKT, and p-4EBP1 were further suppressed by the palbociclib-erlotinib combination (PE-combination) compared with the single-agent treatment (Fig. 5G). KEGG analysis of the RNA-seq data from PIK3CA H1047R LOVO cells received palbociclib or PE-combination treatment revealed that the cell cycle was the top enriched pathway (Fig. 5H), and most of the expression of genes in the cell cycle pathway (84 genes were selected in correspondence with the heatmap in Fig. S3E) were downregulated by PE-combination compared with

palbociclib-treatment (Fig. 5I). The above evidence suggested that erlotinib synergizes with palbociclib mainly via inhibition of cell cycle progression, so next we examined the impact of various treatments on cell cycle. As shown in Fig. 5J and K (DLD1 and HCT15 cells) and Fig. S5E and F (PIK3CA MUT LOVO cells), PE-combination resulted in a significantly higher proportion of PIK3CA mutant cells arrested in the G1 phase than palbociclib-treatment. Moreover, PIK3CA mutant cells that received PE-combination underwent more apoptosis than palbociclib or erlotinib single-agent treatment (Fig. 5L and M, Fig. S5G and H).

Cetuximab, a monoclonal antibody targeting the EGFR, was approved by the FDA for metastatic colorectal cancer (CRC) and KRAS wild-type CRC in 2004 and 2009, respectively (28,29). We wondered whether it could also synergize with palbociclib in treating PIK3CA mutant CRC cells since it also targets EGFR. As shown in Fig. S6A and B, the HSA and CI analysis revealed that the interactions between palbociclib and cetuximab were mostly synergistic when they combined at various concentrations, suggesting their interaction were also synergistic. Unfortunately, the antiproliferative activity of cetuximab alone (Fig. S6C) or in combination with palbociclib (Fig. S6D) was moderate in various CRC cell lines since 50% inhibition of the CRC cells' proliferation was hardly achieved even at relatively high concentrations of these two agents (e.g. cetuximab:50 μg/mL; palbociclib: 1 μM) (Fig S6E). Nevertheless, raising the concentration of cetuximab in combination of palbociclib resulted in obvious inhibition of colony formation in CRC cells (including PIK3CA WT HT29 and mutant DLD1 and HCT116 cell lines, Fig. S6F). Given that the overall performance of the palbociclib and cetuximab combination was less potent than that of the palbociclib and erlotinib combination, cetuximab was not selected for the subsequent efficacy study.

6. Combination therapy of palbociclib and erlotinib exhibited significant efficacy in PIK3CA mutant/WT CRC CDX and PDX models.

To evaluate the efficacy of the PE-combination therapy *in vivo*, we first established PIK3CA mutant CRC PDX models in zebrafish or mice. The tumor tissue transplanted into the 48 hpf Tg (flk1:EGFP) zebrafish embryos or 6-8 weeks immunodeficient NNG mice originated from a 47-year male patient (Ca-2021-6-16, abbr. 616#) diagnosed with papillary adenomas of the rectum at June 2021 and carried a H1047L (gain-of-function) mutation in the PIK3CA gene (Fig. S7A). For the PDX zebrafish model, the PE-combination treatment (palbociclib: 0.5 μM; erlotinib: 1 μM) significantly

inhibited the growth of PIK3CA mutant CRC xenograft while neither palbociclib nor erlotinib alone exhibited statistically meaningful difference relative to the control (Fig. 6A and B). For the PDX mouse model, palbociclib (p.o. 25 mg/kg; 3 weeks) alone exerted modest inhibitory effect on 616# tumor growth after two-week treatment (Fig. 6C), but it failed to translate into a meaningful prolongation in overall survival (Fig. 6D). In contrast, the PE-combination treatment (palbociclib: p.o. 25 mg/kg; erlotinib: p.o. 25 mg/kg; 3 weeks) successfully controlled the PIK3CA mutant tumor growth, caused remarkable reduction of tumor volume (Fig. 6C and G), and resulted into markedly prolonged survival compared with both the vehicle-treated and palbociclib-treated PDX mice (Fig. 6D). In addition, we also established PDO model with the tumor tissue from the same patient, and the efficacy study again confirmed the effectiveness of the PE-combination (Fig. S7B; palbociclib: 1 μM, erlotinib: 10 μM).

We then performed the β-galactosidase staining and immunohistochemical staining with LCN2 and EGFR antibodies on the tumor tissue samples from different treatment groups in the PDX mouse model. The results confirmed that palbociclib treatment rendered increased expression of β-galactosidase as well as LCN2 and EGFR. Interestingly, the number of β-galactosidase-positive senescent cells was less in the tumors collected from the PE-combination treated group than in the palbociclib-treated group, possibly due to substantial apoptosis caused by the combined treatment. Because erlotinib blocks the activity of EGFR by binding to its tyrosine kinase domain, the expression of EGFR was not reduced by the PE-combination treatment (Fig. 6E and F). In addition, we again observed the colocalization of EGFR and LCN2 in the PDX tumor tissues being immunofluorescence stained with anti-EGFR and anti-LCN2, indicating the direct binding of the two proteins (Fig. 6H).

As the PIK3CA mutant DLD1 cells were refractory to palbociclib *in vitro*, we also evaluated the *in vivo* efficacy of palbociclib and the PE-combination treatment in a DLD1 xenograft model. Again, the single-agent treatment of palbociclib failed to effectively inhibit the tumor growth and prolong the survival of treated mice, whereas the PE-combination treatment resulted in significant tumor suppression and survival prolongation (Fig. S7C-E).

Lastly, we wanted to know whether the PE-combination therapy was also effective for PIK3CA WT CRC. To investigate it, tumor tissue derived from a tubulopapillary rectal adenocarcinoma from a 26-year female patient (Ca-18-4-4, abbr. 44#) was transplanted into immunodeficient NNG mice to generate a PDX model. The following sequencing revealed that it contained the WT PIK3CA gene together with the KRAS G13D mutant gene (Fig. S7A). Unlike the above PI3K mutant PDX model,

palbociclib alone was sufficient to cause meaningful tumor suppression and improvement of overall survival in this PIK3CA WT; KRAS G13D mutant CRC PDX model (Fig. 6I-K). Even so, the PE-combination treatment exhibited a stronger therapeutic effect than palbociclib alone, and resulted in dramatic tumor suppression and markedly prolonged survival, suggesting that the PE-combination therapy can also be a potent and effective treatment for PIK3CA WT CRC. In addition, the H&E and Ki-67 staining of tumor tissue from the DLD1 xenograft model, 616# and 44# model consistently demonstrated that the PE-combination treatment was able to efficiently eliminate massive quick proliferative tumor cells in comparison with the vehicle-treatment, while the single-agent treatment by palbociclib or erlotinib failed to do so (Fig. S7F-H). Notably, all mice received this clinically relevant dosage of the PE-combination (palbociclib: p.o. 25 mg/kg; erlotinib: p.o. 25 mg/kg) did not show any severe toxicity or side effect, suggesting it is a safe therapeutic intervention (Fig. S7I).

DISCUSSION

Palbociclib is an excellent CDK4/6 inhibitor, but so far its clinical application is mainly limited to the treatment of ER/HR-positive and HER2-negative metastatic breast cancer. Recent works discovered that the mechanism of action of palbociclib and other CDK4/6 inhibitors may not be as simple as once thought. The consequent biological effects after CDK4/6 inhibition include but are not limited to induction of cellular senescence and apoptosis, alteration of cellular metabolism, and remodeling tumor microenvironment (30), and the therapeutic potential of palbociclib in the treatment of various types of cancer is yet to be excavated.

In the present study, we demonstrated that palbociclib could cause divergent responses in CRC cells depending on their distinct genetic backgrounds. Compared with PIK3CA WT cells, palbociclib treatment led to a strong SASP and altered secretion of SASP factors in CRC cells harboring the gain-of-function mutation of PIK3CA (e.g. E545K and H1047R), and this phenotype was identified as a major contributor to the palbociclib resistance. Mechanistically, the excessively secreted SASP factor LCN2 blocked the lysosome-mediated degradation of EGFR in the surrounding non-senescent CRC cells, and the overexpressed EGFR rendered upregulation of multiple palbociclib-resistance genes. Importantly, the SASP-induced resistance could be overcome by the addition of erlotinib, an EGFR inhibitor. Eventually, the combination therapy of palbociclib and erlotinib significantly suppressed the proliferation and induced apoptosis in PIK3CA mutant CRC cells and exhibited potent efficacy and

excellent safety in PDO/PDX/CDX models (Fig. 6 and S7).

It is noteworthy that two early studies also reported that the efficacy of palbociclib could be compromised by the PIK3CA mutation in oral squamous cell carcinoma and melanoma (31,32). Although the mechanism in these studies was either not completely elucidated or inconsistent with ours, these authors probably observed a general phenomenon as we observed. Tumor cells with OIS have adapted to a pre-senescent state, so when a proportion of these cells were finally pushed into the terminal state of senescence by palbociclib or other drugs with TIS activity, a survival signal could be triggered and transmitted via the secretion of SASP factors to counterbalance the senescence pressure caused by CDK4/6 inhibition. If the survival signal ultimately causes the activation or elevation of strong driver proteins such as EGFR, then it would not only promote drug resistance but also lead to the constant proliferation and division of tumor cells. From the perspective of tumor evolution, this change appears to be an adaptive mechanism by which the stress of cell cycle arrest and cellular senescence on the whole tumor cell community can be greatly alleviated.

Furthermore, we postulated that this phenomenon is not only limited to the PIK3CA-mutation-induced senescence but also can be extended to the OIS caused by mutation of other oncogenes, such as KRAS and PTEN. If this hypothesis is true, OIS could play a critical role not only in drug resistance but also in tumor development, metastasis, and recurrence as long as senescence-induced therapy is given. Except for the tumor cells, what impact could be caused by the OIS-induced altered expression of SASP factors on the tumor microenvironment consisting of stromal cells, vascular cells, and immune cells is completely unknown. Therefore, more investigations are required to study the response of tumor cells with these genotypes when they confront senescence-induced therapy including but not limited to CDK4/6 targeted therapy, chemotherapy, and radiotherapy.

It is worth mentioning that LCN2 is probably not the only SASP factor that was involved in the upregulation of EGFR in this study. As shown in Fig. S4C, there were at least 11 SASP factors that had strong interactions with EGFR besides LCN2, and some of them had been previously reported to be able to upregulate the expression of EGFR, e.g. mucin 1 encoded by MUC1(33-35), IGFBP-1 encoded by IGFBP1 (36), TNF-α encoded by TNF (37). Therefore, multiple SASP factors secreted by senescent PI3KCA mutant CRC cells might have been involved and they collaboratively promoted the elevation of EGFR and consequently caused palbociclib resistance. In this sense, an optimal therapeutic effect

might not be achieved if we solely blocked the activity or expression of LCN2. Instead, EGFR is a crucial regulator in the oncogenesis and progression of various malignancies and plays a significant role in mediating drug resistance including CDK4/6 inhibitors (38), so it provides a better target to overcome the palbociclib resistance in PIK3CA mutant CRC. Moreover, our results also demonstrated that the combination therapy of CDK4/6 and EGFR inhibitors were both effective for PIK3CA mutant and WT CRC, so it may represent a general therapeutic approach for CRCs across different genotypes.

The EGFR monoclonal antibody drug cetuximab is an FDA-approved targeted therapeutic for the first-line treatment of RAS-WT metastatic CRC. Despite that it also exhibited synergistic interaction with palbociclib, the overall anti-CRC potency of the cetuximab and palbociclib was limited in the treatment of PIK3CA mutant CRC cells in our study. Coincidentally, a recent clinical study also showed that a combination therapy consisting of cetuximab and palbociclib failed to achieve significant improvement in the treatment of patients with KRAS-WT metastatic CRC (5). The underlying mechanism for these findings could be complicated, but one potential explanation is that cetuximab lacks the capacity of erlotinib to inhibit the activity of intracellular EGFR which can be still activated and functioning as an oncoprotein (39).

In this study, we found that the PIK3CA mutant CRCs were refractory to palbociclib treatment. It is important information for future trials in which palbociclib will be involved. Just as the patients with triple-negative breast cancers could not benefit from the palbociclib, it would be reasonable that only a subgroup of CRC patients is suitable for the palbociclib treatment as well. Therefore, our study highlights the importance of identifying the potential treatment-beneficial/refractory subgroup(s) when a targeted therapeutic agent is involved. Finally, we recently initiated a project aiming to develop a CDK4/6 and EGFR multi-targeting inhibitor using a pharmacophore fusion strategy, and have identified several candidate compounds with promising activities. It is anticipated that these efforts together will eventually translate into effective therapeutic solutions that benefit CRC patients even if they are in a treatment-refractory subgroup.

Data Availability

The RNA-seq data have been deposited in the Gene Expression Omnibus (GEO) and are publicly accessible as of the publication date, under the accession number GSE276620.

Authors' Disclosures

The authors declare no competing interests.

Acknowledgments

This work is supported by the National Natural Science Foundation of China (81672962 and 21905138), the National Natural Science Youth Foundation of China (82303894), the Natural Science Foundation of Jiangsu Province (BK20220311), the Jiangsu Provincial Innovation Team Program Foundation, and the Joint Key Project Foundation of Southeast University and Nanjing Medical University. We thank Dr. Jianmin Li, Dr. Yujie Sun and Dr. Xuerong Wang for their valuable advice and support on this project.

REFERENCES

1. Sung H, Ferlay J, Siegel RL, Laversanne M, Soerjomataram I, Jemal A, et al. Global Cancer Statistics 2020: GLOBOCAN Estimates of Incidence and Mortality Worldwide for 36 Cancers in 185 Countries. CA Cancer J Clin 2021;71(3):209-49
2. Biller LH, Schrag D. Diagnosis and Treatment of Metastatic Colorectal Cancer: A Review. JAMA 2021;325(7):669-85
3. Beaver JA, Amiri-Kordestani L, Charlab R, Chen W, Palmby T, Tilley A, et al. FDA Approval: Palbociclib for the Treatment of Postmenopausal Patients with Estrogen Receptor-Positive, HER2-Negative Metastatic Breast Cancer. Clin Cancer Res 2015;21(21):4760-6
4. Sorah JD, Moore DT, Reilley MJ, Salem ME, Triglianos T, Sanoff HK, et al. Phase II Single-Arm Study of Palbociclib and Cetuximab Rechallenge in Patients with KRAS/NRAS/BRAF Wild-Type Colorectal Cancer. Oncologist 2022;27(12):1006-e930
5. Sorah JD, Moore DT, Reilley MJ, Salem ME, Triglianos T, Sanoff HK, et al. Phase II Single-Arm Study of Palbociclib and Cetuximab Rechallenge in Patients with Wild-Type Colorectal Cancer. Oncologist 2022;27(12):1006-E930
6. Matthews HK, Bertoli C, de Bruin RAM. Cell cycle control in cancer. Nat Rev Mol Cell Biol 2022;23(1):74-88
7. Goel S, Bergholz JS, Zhao JJ. Targeting CDK4 and CDK6 in cancer. Nat Rev Cancer 2022;22(6):356-72

8. Thoma OM, Neurath MF, Waldner MJ. Cyclin-Dependent Kinase Inhibitors and Their Therapeutic Potential in Colorectal Cancer Treatment. Front Pharmacol 2021;12:757120
9. Goel S, DeCristo MJ, McAllister SS, Zhao JJ. CDK4/6 Inhibition in Cancer: Beyond Cell Cycle Arrest. Trends Cell Biol 2018;28(11):911-25
10. Wang B, Varela-Eirin M, Brandenburg SM, Hernandez-Segura A, van Vliet T, Jongbloed EM, et al. Pharmacological CDK4/6 inhibition reveals a p53-dependent senescent state with restricted toxicity. EMBO J 2022;41(6):e108946
11. Vijayaraghavan S, Karakas C, Doostan I, Chen X, Bui T, Yi M, et al. CDK4/6 and autophagy inhibitors synergistically induce senescence in Rb positive cytoplasmic cyclin E negative cancers. Nat Commun 2017;8:15916
12. Rossiello F, Jurk D, Passos JF, d'Adda di Fagagna F. Telomere dysfunction in ageing and age-related diseases. Nat Cell Biol 2022;24(2):135-47
13. Ou HL, Hoffmann R, Gonzalez-Lopez C, Doherty GJ, Korkola JE, Munoz-Espin D. Cellular senescence in cancer: from mechanisms to detection. Mol Oncol 2021;15(10):2634-71
14. Guillon J, Petit C, Toutain B, Guette C, Lelievre E, Coqueret O. Chemotherapy-induced senescence, an adaptive mechanism driving resistance and tumor heterogeneity. Cell Cycle 2019;18(19):2385-97
15. Zhu H, Blake S, Kusuma FK, Pearson RB, Kang J, Chan KT. Oncogene-induced senescence: From biology to therapy. Mech Ageing Dev 2020;187:111229
16. Schmitt CA, Wang BS, Demaria M. Senescence and cancer - role and therapeutic opportunities. Nat Rev Clin Oncol 2022;19(10):619-36
17. Faget DV, Ren Q, Stewart SA. Unmasking senescence: context-dependent effects of SASP in cancer. Nat Rev Cancer 2019;19(8):439-53
18. Birch J, Gil J. Senescence and the SASP: many therapeutic avenues. Gene Dev 2020;34(23-24):1565-76
19. Courlet P, Cardoso E, Bandiera C, Stravodimou A, Zurcher JP, Chtioui H, et al. Population Pharmacokinetics of Palbociclib and Its Correlation with Clinical Efficacy and Safety in Patients with Advanced Breast Cancer. Pharmaceutics 2022;14(7)
20. Tan JX, Finkel T. Lysosomes in senescence and aging. EMBO Rep 2023;24(11):e57265
21. Guerrero-Navarro L, Jansen-Durr P, Cavinato M. Age-Related Lysosomal Dysfunctions. Cells 2022;11(12)
22. Lasry A, Ben-Neriah Y. Senescence-associated inflammatory responses: aging and cancer perspectives. Trends Immunol 2015;36(4):217-28
23. Chen C, Jing W, Chen Y, Wang G, Abdalla M, Gao L, et al. Intracavity generation of glioma stem cell-specific CAR macrophages primes locoregional immunity for postoperative glioblastoma therapy. Science translational medicine 2022;14(656):eabn1128
24. Park YH, Im SA, Park K, Wen J, Lee KH, Choi YL, et al. Longitudinal multi-omics study of palbociclib resistance in HR-positive/HER2-negative metastatic breast cancer. Genome Med 2023;15(1)
25. Yammine L, Zablocki A, Baron W, Terzi F, Gallazzini M. Lipocalin-2 Regulates Epidermal

Growth Factor Receptor Intracellular Trafficking. Cell Rep 2019;29(7):2067-77 e6
26. Alwan HAJ, van Leeuwen JEM. UBPY-mediated epidermal growth factor receptor (EGFR) de-ubiquitination promotes EGFR degradation. Journal of Biological Chemistry 2007;282(3):1658-69
27. Chen Z, Chen C, Zhou T, Duan C, Wang Q, Zhou X, et al. A high-throughput drug combination screen identifies an anti-glioma synergism between TH588 and PI3K inhibitors. Cancer Cell Int 2020;20:337
28. Goldberg RM. Cetuximab. Nat Rev Drug Discov 2005;Suppl:S10-1
29. Goldberg RM, Venook AP, Schilsky RL. Cetuximab in the treatment of colorectal cancer. Clin Adv Hematol Oncol 2004;2(11):1-10; quiz 1-2
30. Klein ME, Kovatcheva M, Davis LE, Tap WD, Koff A. CDK4/6 Inhibitors: The Mechanism of Action May Not Be as Simple as Once Thought. Cancer Cell 2018;34(1):9-20
31. Romano G, Chen PL, Song P, McQuade JL, Liang RJ, Liu MG, et al. A Preexisting Rare Subpopulation Confers Clinical Resistance to MEK plus CDK4/6 Inhibition in Melanoma and Is Dependent on S6K1 Signaling. Cancer Discovery 2018;8(5):556-67
32. Zainal NS, Lee BKB, Wong ZW, Chin IS, Yee PS, Gan CP, et al. Effects of palbociclib on oral squamous cell carcinoma and the role of PIK3CA in conferring resistance. Cancer Biol Med 2019;16(2):264-75
33. Ma QX, Song JY, Wang S, He NN. MUC1 regulates AKT signaling pathway by upregulating EGFR expression in ovarian cancer cells. Pathol Res Pract 2021;224
34. Engel BJ, Bowser JL, Broaddus RR, Carson DD. MUC1 stimulates EGFR expression and function in endometrial cancer. Oncotarget 2016;7(22):32796-809
35. Tong F, Zhao JX, Fang ZY, Cui XT, Su DY, Liu X, et al. MUC1 promotes glioblastoma progression and TMZ resistance by stabilizing EGFRvIII. Pharmacol Res 2023;187
36. Zheng Y, Sowers JY, Houston KD. IGFBP-1 Expression Promotes Tamoxifen Resistance in Breast Cancer Cells via Erk Pathway Activation. Front Endocrinol 2020;11
37. Yoo J, Perez CER, Nie WX, Edwards RA, Sinnett-Smith J, Rozengurt E. TNF-α induces upregulation of EGFR expression and signaling in human colonic myofibroblasts. Am J Physiol-Gastr L 2012;302(8):G805-G14
38. Belli S, Esposito D, Ascione CM, Messina F, Napolitano F, Servetto A, et al. EGFR and HER2 hyper-activation mediates resistance to endocrine therapy and CDK4/6 inhibitors in ER plus breast cancer. Cancer Letters 2024;593
39. Burke P, Schooler K, Wiley HS. Regulation of epidermal growth factor receptor signaling by endocytosis and intracellular trafficking. Mol Biol Cell 2001;12(6):1897-910
40. Demichev V, Messner CB, Vernardis SI, Lilley KS, Ralser M. DIA-NN: neural networks and interference correction enable deep proteome coverage in high throughput. Nat Methods 2020;17(1):41-4
41. Koo BK, Stange DE, Sato T, Karthaus W, Farin HF, Huch M, et al. Controlled gene expression in primary Lgr5 organoid cultures. Nat Methods 2011;9(1):81-3

Methods

REAGENT or RESOURCE	SOURCE	IDENTIFIER
Antibodies		
EGF Receptor (D38B1) XP® Rabbit mAb	Cell Signaling Technology	#4267 RRID:AB_2246311
Phospho-EGF Receptor (Tyr1068) (D7A5) XP® Rabbit mAb	Cell Signaling Technology	#3777 RRID:AB_2096270
Phospho-Akt (Ser473) (D9E) XP® Rabbit mAb	Cell Signaling Technology	#4060 RRID:AB_2315049
Phospho-Akt (Thr308) (D25E6) XP® Rabbit mAb	Cell Signaling Technology	#13038 RRID:AB_2629447
Phospho-p44/42 MAPK (Erk1/2) (Thr202/Tyr204) (D13.14.4E) XP® Rabbit mAb	Cell Signaling Technology	#4370 RRID:AB_2315112
Phospho-MEK1/2 (Ser221) (166F8) Rabbit mAb	Cell Signaling Technology	#2338 RRID:AB_490903
Phospho-Rb (Ser807/811) (D20B12) XP® Rabbit mAb	Cell Signaling Technology	#8516 RRID:AB_11178658
Rb (4H1) Mouse mAb	Cell Signaling Technology	#9309 RRID:AB_823629
GSK-3β (D5C5Z) XP® Rabbit mAb	Cell Signaling Technology	#12456 RRID:AB_2636978
Phospho-GSK-3β (Ser9) (5B3) Rabbit mAb	Cell Signaling Technology	#9323 RRID:AB_2115201
FoxM1 (D12D5) XP® Rabbit mAb	Cell Signaling Technology	#5436 RRID:AB_10692483
Lipocalin-2 Antibody	Aifang	AF301156 RRID:AB_3644233
p-4E-BP1 Antibody (62.Ser	Santa Cruz Biotechnology	SC293124 RRID:AB_2943677

65)		
Affinity Gel-conjugated Mouse anti DDDDK-Tag mAb	ABclonal	AE061 RRID:AB_2863789
GAPDH Mouse mAb (AC002)	ABclonal	#AC002 RRID:AB_2736879
β-actin,Mouse mAb	Yeasen	30101ES10 RRID: AB_3644235
Goat anti-Rabbit IgG-Cy3 Antibody	Absin	abs20024 RRID: AB_3644236
Goat anti-Mouse IgG-FITC Antibody	Absin	abs20012 RRID: AB_3644238
Chemicals		
Palbociclib (HY-50767)	MedChemExpress Chemicals	HY-50767
Erlotinib	MedChemExpress Chemicals	HY-50896
Cycloheximide	MedChemExpress Chemicals	HY-12320
leupeptin	MedChemExpress Chemicals	HY-18234
Actinomycin D	MedChemExpress Chemicals	HY-17559
A 83-01	MedChemExpress Chemicals	HY-10432
SB 202190	MedChemExpress Chemicals	HY-10295
Y-27632	MedChemExpress Chemicals	HY-10071
Corning® Matrigel®	Corning	354230
collagenase A	Sigma	C0130
N-Acetylcysteine	Sigma	A0737
HEPES (1 M)	Gibco	15630080
GlutaMAX™	Gibco	35050061
B-27™	Gibco	17504044
N-2	Gibco	17502001
Human EGF Recombinant Protein	Thermo Fisher Scientific	#PHG0313

Commercial assays		
DAPI Fluoromount-G™	Yeasen	36308ES11
Membrane and Cytosol Protein Extraction Kit	Yeasen	20127ES50
Cell Counting Kit (CCK-8) CCK-8	Yeasen	40203ES88
BCA Protein Quantification Kit（Ready to use）	Yeasen	20200ES76
Human lipocalin-2 (LCN-2) ELISA Kit.	Aifang	AF1983-A
Human TGF-α ELISA Kit.	Aifang	AF0090-A
Software		
Prism 8	Graphpad	https://www.graphpad.com/
FlowJo 7.6	Treestar	https://www.flowjo.com/
ImageJ	Freeware/NIH	https://imagej.nih.gov/ij/
GSEA	GSEA	https://www.gsea-msigdb.org/gsea
Primers for q-PCR		
gene name	Forward primer	Reverse primer
GAPDH	AATCCCATCACCATCTTCC	CATCACGCCACAGTTTCC
CCL2	GCCTCCAGCATGAAAGTCTC	CAGATCTCCTTGGCCACAAT
CCL11	CCCCTTCAGCGACTAGAGAG	TCTTGGGGTCGGCACAGAT
IL6	AACCTGAACCTTCCAAAGATGG	TCTGGCTTGTTCCTCACTACT
IL10	GCCTAACATGCTTCGAGATC	TGATGTCTGGGTCTTGGTTC
CXCL5	AGCTGCGTTGCGTTTGTTTAC	TGGCGAACACTTGCAGATTAC

CXCL8	CACTGCGCCAACACAGAAAT	GCCCTCTTCAAAAACTTCTCCAC
TGFA	TCGCTCTGGGTATTGTGTTG	GACCTGGCAGCAGTGTATCA
TGFB1	TGGCGATACCTCAGCAAC	ACCCGTTGATGTCCACTTG
MMP1	CTTGCACTGAGAAAGAAGACAAAGG	ACACCCCAGAACAGCAGCA
EGFR	AGGCACGAGTAACAAGCTCAC	ATGAGGACATAACCAGCCACC
LCN2	CCACCTCAGACCTGATCCCA	CCCCTGGAATTGGTTGTCCTG

Cell lines

Human colorectal cancer (CRC) cell lines, including SW620, HCT116, HCT15, DLD1, and LOVO, were procured from the Cell Bank of the Chinese Academy of Sciences, located in Shanghai, China. Authentication of these cell lines was conducted by Biowing Biotech, also based in Shanghai, China. The SW620, HCT116, and LOVO cell lines were maintained in Dulbecco's Modified Eagle Medium (DMEM; Gibco, CA, USA), supplemented with 10% fetal bovine serum (FBS; TransGen, Beijing, China) and 100 μg/mL penicillin/streptomycin (Invitrogen, CA, USA). The remaining cell lines, HCT15 and DLD1, were cultured in RPMI-1640 medium (Gibco, CA, USA) with identical supplements. All cells were cultured in a humidified incubator with 5% carbon dioxide (CO_2) and 95% air at 37 °C and were routinely checked for mycoplasma by PCR analysis.

Plasmid construction

The lentiviral vector for the PIK3CA gene, specifically targeting the E545K and H1047R mutation sites, was developed through a systematic approach. Initially, the expression vector plvx, containing the full-length open reading frame of the human wild-type PIK3CA, was synthesized and amplified via polymerase chain reaction (PCR). Subsequently, plasmids harboring the E545K and H1047R point mutations were generated using the homologous recombination technique, facilitated by the CloneExpress Ultra One Step Cloning Kit (Vazyme, Nanjing, China), in accordance with the manufacturer's guidelines.

Lentivirus production and infection

HEK293T cells were seeded into 12-well dishes at a density of 5 × 10^6 cells per dish and incubated for 24 hours prior to transfection. Once the cells reached 60%–70% confluence, a transfection mixture containing the envelope vector pVSVG and the packaging vector psPAX2 was introduced to each dish. 18 hours post-transfection, the medium was replaced with a fresh culture medium. After an additional 48 hours, the supernatant containing the lentivirus was collected and filtered through a 0.45 μm low protein-binding membrane. Subsequently, the culture medium for LOVO and SW620 cells designated for infection was substituted with the previously described lentivirus-containing supernatant. Polyene was introduced at a dilution of 1:1000, and the mixture was subjected to centrifugation at 37°C for 2 hours to facilitate viral infection. Following this, a puromycin selection period of 3 to 7 days was implemented, after which the infected cells were harvested for DNA and protein extraction. Sanger sequencing and Western blotting (WB) analyses were conducted to confirm PIK3CA mutations and the overexpression of the EGFR or LCN2 genes.

Collection of conditioned media (CM)

LOVO cells were seeded in 10-cm culture dishes and cultured overnight. Subsequently, they were treated with 0.5 μM palbociclib and maintained in a CO_2 incubator for 3 days. Following this incubation period, the cells were washed with PBS and incubated in a fresh medium. After 48 hours, the cell supernatant was collected and centrifuged at 3000 rpm for five minutes to remove debris. The supernatant was then aliquoted and stored in a -80 °C freezer. This preparation was designated as the senescent cell-conditioned medium (S-CM), with the conditioned medium treated with DMSO serving as the control.

Clonogenic assays

Colorectal cancer (CRC) cells were cultured in 12-well plates at a seeding density of 500 to 1000 cells per well. The medium, either containing the drug or fresh, was replenished every 3 to 4 days. Following an incubation period of 10 to 14 days, the resulting colonies were washed with phosphate-buffered saline (PBS), fixed using 4% paraformaldehyde for 15 minutes, and subsequently stained with Giemsa Stain solution (KeyGEN, Nanjing, China).

Proliferation and anti-proliferation assays

Colorectal cancer (CRC) cells were seeded into 96-well plates at a density of 1,000 to 3,000 cells per well and cultured for 24 hours. Subsequently, the cells were exposed to varying concentrations of

drugs or different formulations, specifically palbociclib and erlotinib, at equivalent drug concentrations for a duration of 72 hours. Following this treatment period, the medium was aspirated, and a fresh medium containing CCK8 (10 μL per well) was added (Yeasen, Shanghai, China). After an additional incubation period of 1 to 4 hours, the optical density at 450 nm for each well was measured using a microplate reader. The resulting data were analyzed utilizing GraphPad Prism software.

RNA extraction and quantitative real-time PCR assay (qRT-PCR)

Total RNA was extracted utilizing the Trizol reagent (Takara, Japan) in accordance with the manufacturer's protocol. Subsequently, 1000 ng of RNA was reverse-transcribed to synthesize complementary DNA (cDNA), following the instructions provided by Takara. Quantitative real-time polymerase chain reaction (qRT-PCR) was conducted using the SYBR Green q-PCR mix (Yeasen, Shanghai, China) to detect PCR products. The thermal cycling conditions were as follows: an initial denaturation at 95 °C for 10 minutes, followed by 40 cycles of denaturation at 95 °C for 15 seconds, annealing at 60 °C for 15 seconds, and extension at 72 °C for 15 seconds. The mRNA levels of the genes were normalized to GAPDH and calculated using the 2^(-ΔΔCt) method, and the data were analyzed using GraphPad Prism software.

Western blotting

Cells were lysed using RIPA buffer supplemented with protease inhibitors, comprising 50 mmol/L Tris-HCl at pH 8.0, 150 mM sodium chloride, 1.0% NP-40, 0.5% sodium deoxycholate, and 0.1% SDS. Protein concentrations were quantified utilizing the BCA Protein Assay Kit (Yeasen, Shanghai, China). Subsequently, equal amounts of protein (10-20 μg) were subjected to SDS-PAGE for electrophoretic separation. Following electrophoresis, proteins were transferred onto a PVDF membrane (Merck Millipore, MA, USA). The membrane was then blocked with 3% BSA and incubated with appropriate primary and secondary antibodies. Imaging of the membranes was conducted using a Tanon Imager (Tanon, Shanghai, China).

RNA sequencing

Library construction and RNA sequencing were performed following the extraction of total RNA from the cells using the TRIzol® Reagent, adhering to the manufacturer's protocol (Invitrogen). The assessment of RNA quality and subsequent sequencing were carried out by BGI (Beijing, China). Comprehensive experimental methodologies, along with the raw data and gene expression profiles, have been deposited in the GEO database (https://www.ncbi.nlm.nih.gov/gds) and are accessible under

the accession number GSE276620.

Mass spectrometry analysis

Cells were lysed utilizing an 8 M urea solution in 50 mM Tris buffer, supplemented with a protease inhibitor cocktail. This was followed by sonication to ensure complete disruption. Subsequently, cellular debris was eliminated through centrifugation at 20,000 g for 30 minutes at 4 °C. Protein concentration was quantified using the Bradford assay. A total of 100 μg of protein was subjected to reduction with dithiothreitol (DTT), alkylation with iodoacetamide, and enzymatic digestion with trypsin at a concentration of 10 ng/μL (Promega, USA). The digested peptides underwent desalting using C18 columns (Waters) and were subsequently dried utilizing a SpeedVac concentrator. The peptides were then separated on a self-packed C18 analytical column measuring 75 μm × 16 cm, with a particle size of 1.9 μm (Dr. Maisch GmbH, Germany), employing the Easy-nLC 1200 system (Thermo Fisher, USA). The analysis was conducted using an Orbitrap Fusion Lumos Tribrid mass spectrometer (Thermo Fisher, USA). The data-independent acquisition (DIA) mode was employed, with MS1 data acquired in the Orbitrap mass spectrometer over a mass range of 350-1500 m/z at a resolution of 120,000. MS/MS analysis was conducted using high-energy collision dissociation (HCD) in the Orbitrap at a resolution of 30,000. The resulting DIA files were analyzed in a library-free manner using DIA-NN version 1.8 (40), referencing the human UniProt sequence database (release 2023_05) with default parameters. The false discovery rate (FDR) was controlled at 1% through a target-decoy approach at both the peptide and protein levels.

ELISA assays

Following a 72-hour treatment of LOVO cells with palbociclib, the culture medium was refreshed. Subsequently, after an additional 48-hour period, the concentrations of LCN2 and TGF-α proteins present in the cell supernatant were quantified utilizing ELISA kits (Aifang, Wuhan, China) following the manufacturer's protocol. Data visualization was performed using GraphPad Prism software.

Co-immunoprecipitation experiments

Immunoprecipitation assays were conducted on 293T and LOVO cell lines. For these experiments, 5 μg each of LCN2-Flag and EGFR-Flag plasmids were co-transfected into the cells using polyethyleneimine (PEI) as the transfection reagent. After a 48-hour incubation period post-transfection, the cells were lysed in a buffer solution comprising 50 mM Tris, 150 mM NaCl, and 0.1%-0.5% detergent (Triton X-100, Tween 20, or NP-40) at pH 7.5. The lysates were then incubated on ice for 20

minutes and subsequently centrifuged at 12,000 rpm for 15 minutes. The resulting supernatant was collected for immunoprecipitation, which was performed overnight at 4 °C using antibodies specific to EGFR and LCN2, with rabbit IgG employed as a negative control. The subsequent day, magnetic beads (Protein A/G Magnetic Beads for IP, Selleck, USA) were introduced to the mixture, which was then incubated for an additional 2 hours at 4 °C. Following incubation, the beads were washed, and the proteins were eluted and denatured. SDS-PAGE electrophoresis was subsequently conducted. The presence of LCN2 and EGFR in the precipitates was determined via Western blot analysis employing an anti-Flag monoclonal murine antibody.

Cell immunofluorescence

Immunofluorescence analysis was conducted on LOVO and SW620 cell lines. LCN2-Flag and EGFR-Flag plasmids, each at a concentration of 5 μg, were co-transfected into 293T and LOVO cells utilizing polyethyleneimine (PEI) as the transfection agent. Forty-eight hours post-transfection, the cells were fixed for one hour in a solution of 5% bovine serum albumin (BSA) in phosphate-buffered saline (PBS). Subsequently, the cells were incubated overnight with primary antibodies targeting LCN2 and EGFR. This was followed by a 2 hour incubation at room temperature with fluorescently labeled secondary antibodies: Goat anti-Rabbit IgG-Cy3 and Goat anti-Mouse IgG-FITC (Absin, Shanghai, China). Finally, the slides were mounted using a DAPI-containing mounting medium (Yeasen, Shanghai, China). Image using a confocal microscope and perform colocalization analysis with ImageJ software.

Membrane protein extraction

LOVO and SW620 cells, which were stably transfected with the LCN2 gene (1×10^6 cells), were harvested and washed withPBS. The cells were then detached from the culture dish through scraping. Following this, the cells were subjected to centrifugation at 200 × g for 5 minutes at 4°C to obtain the cell pellet. Proteins were subsequently extracted from the cell membrane and cytoplasm utilizing the membrane and cytoplasm protein extraction kit (Yeasen, Shanghai, China) in accordance with the manufacturer's instructions. The isolated proteins were then subjected to western blotting and functional analysis.

Ubiquitination assays

HEK 293T cells were co-transfected with plasmids encoding EGFR-flag, LCN2-flag, and HA-Ubiquitin to assess the ubiquitination of exogenous EGFR. After 48 hours, the cells were lysed in a

buffer comprising 50 mM Tris, 150 mM NaCl, and 0.1%-0.5% detergent (such as Triton X-100, Tween 20, or NP-40), adjusted to pH 7.5. The lysates were incubated on ice for 20 minutes, followed by centrifugation at 12,000 rpm for 15 minutes. The resulting supernatant was subjected to immunoprecipitation overnight at 4 °C using anti-EGFR antibodies. Subsequently, magnetic beads were introduced, and the mixture was further incubated for 2 hours at 4 °C. The Protein A/G Magnetic Beads for immunoprecipitation (Selleck, USA) underwent a washing process, followed by the elution and denaturation of proteins. Subsequently, SDS-PAGE electrophoresis was conducted. The presence of HA, LCN2, and EGFR within the precipitates was determined via Western blot analysis utilizing anti-Flag and anti-HA antibodies.

β-Gal staining

The intracellular levels of β-galactosidase were assessed utilizing a Cell Senescence Testing Kit (GenMed Scientifics, MN, USA), adhering to the protocol provided by the manufacturer. In summary, colorectal cancer (CRC) cells, pre-seeded in 12-well plates, were exposed to palbociclib for a duration of 72 hours. Subsequently, the cells were incubated with the fixative solution, followed by washing and incubation with the Staining Solution for 12-16 hours at 37 °C. Post-incubation, the cells underwent three washes withPBS and were examined using a Zeiss microscope. The number of β-galactosidase-positive cells was quantified across three representative fields from three independent experiments.

Flow Cytometry Analysis of Cell Cycle and Apoptosis

Cells were seeded at a density of 1x10^5 cells per well in 6-well plates and incubated overnight. For cell cycle analysis, synchronization was achieved by serum starvation in serum-free DMEM for 24 hours prior to treatment. Subsequently, the cells were exposed to palbociclib, erlotinib, or their combination for 72 hours. Post-treatment, cells were harvested via trypsinization into ice-cold PBS, followed by brief centrifugation. The resulting cell pellets were fixed in 75% ethanol for 2 hours and then resuspended in 1% (w/v) bovine serum albumin in PBS for cell cycle analysis. Subsequently, the cells were subjected to staining with propidium iodide (PI) at a final concentration of 0.1 mg/mL, in conjunction with 0.1 mg/mL RNaseA (20 g/mL), and incubated at 37 °C for 15 minutes in the absence of light. For the purpose of apoptosis analysis, a total of 1×10^5 treated cells were stained with Annexin V-APC and propidium iodide (PI) utilizing an Apoptosis Detection Kit (Yeasen, Shanghai, China) at ambient temperature for 15 minutes. The resulting data were analyzed using FlowJo software

version 7.6.

Animals

The mice were housed and handled in accordance with institutional guidelines that adhere to local legislation. All animal experiments received approval from the Animal Experiment Committee of Nanjing Medical University. NOD/ShiLtJGpt-*Prkdc*^{em26Cd52}*Il2rg*^{em26Cd22}/Gpt (NNG, Female, 3–4 weeks, 18–20 g) were provided by the local animal center and acclimatized to the laboratory environment for one week prior to the commencement of the experiments. Transgenic zebrafish embryos, Tg(flk1:EGFP), were supplied by Nanjing HuanTe Biotechnology Co., Ltd. (Nanjing, China).

Cell derived xenograft

For the subcutaneous tumor model, LOVO-PIK3CA WT and MUT cells (1.0×10^6) and DLD1 (1×10^6) cell lines into the right flank of each mouse to establish the CRC xenograft model. When the average tumor volume reached about 100-120 mm^3, mice were randomized into various groups for different sets of experiments. The CDX (LOVO-PIK3CA WT and MUT cells) group included 60 tumor-bearing mice (8-10 mice per group). The CDX (LOVO-PIK3CA WT and MUT cells) mouse models were treated with palbociclib [suspended in sodium (S)-lactate buffer (50 mM, pH 4.0); 25 mg/kg], or the combination of the two, 5 days a week for a total of 3 weeks. The CDX (DLD1) group included 20 tumor-bearing mice (5 mice per group). The CDX (DLD1) mouse models were treated with erlotinib (suspended in 6% Captisol; 25 mg/kg), palbociclib [suspended in sodium (S)-lactate buffer (50 mM, pH 4.0); 25 mg/kg], or the combination of the two, 5 days a week for a total of 3 weeks. The mice were weighed, and the tumor size was measured every 2 days, and the tumor volume (length × width^2 × 0.5) was calculated and measured until the tumor reached the ethically allowed maximum volume of 2,000 mm^3 or the health of the mice was seriously deteriorated (censored events).

Patient-derived CRC organoids

CRC specimens were acquired from patients in routine operations after obtaining fully informed consent according to Jiangsu Cancer Hospital. The CRC organoids were established according to the protocol developed by Hans Clevers lab (41). In brief, fresh surgically resected CRC tissues were minced into 1 mm^3 fragments and digested with 1 mg/mL collagenase A (Sigma, USA) at 37 °C for 30 minutes. After a brief centrifugation, the pellet was resuspended in PBS and was mechanically dissociated by repetitive pipetting. The isolated cells/fragments were passed through a 70 μm cell strainer, centrifuged, and resuspended in matrigel (Corning, USA) at 1×10^6 cells per mL. The mixture

was dispensed as 25 μL per drop and seeded into each well in 24-well plates and was solidified in a 37 °C incubator for 10 minutes. 500 μL of culture medium composed of DMEM/F-12 supplemented with 1× penicillin/streptomycin, 10 mM HEPES (Gibco, USA), 2 mM GlutaMAX (Gibco, USA), 1× B27 (Gibco, USA), 1× N2 (Gibco, USA), 1 mM N-Acetylcysteine (Sigma, USA) together with niche factors: 50 ng/mL for EGF (Thermo Fisher Scientific, USA), 500 nM for TGF-β receptor type I inhibitor A83-01 (MCE, Shanghai, China) and 10 μM for p38 MAP kinase inhibitor SB202190 (MCE, Shanghai, China) was added into each well. 10 mM Y-27632 dihydrochloride kinase inhibitor (MCE, Shanghai, China) was also added for the first 2 days. After the successful formation of CRC organoids, palbociclib, erlotinib, or their combination was added into the culture medium to evaluate their effects.

Patient-derived CRC xenografts mouse models

For the PDX mouse model, 4-5 weeks female immunodeficient NNG mice were used as the recipient of patient-derived CRC tissue. Fresh surgically resected CRC tissues from two CRC patients (P616# and P44#) were minced into approximately 0.3 cm^3 fragments and subcutaneously engrafted into the right axillary position of each mouse. When tumors reached a volume of 80-120 mm^3, the mice were separated randomly into 4 groups. The PDX (616#) group included 36 tumor-bearing mice (8-10 mice per group) and the PDX (44#) group included 37 tumor-bearing mice (8-10 mice per group). The PDX mouse models were treated with erlotinib (suspended in 6% Captisol; 25 mg/kg), palbociclib [suspended in sodium (S)-lactate buffer (50 mM, pH 4.0); 25 mg/kg], or the combination of the two, 5 days a week for a total of 3 weeks. The mice were weighed and the tumor size was measured every 2 days, and the tumor volume (length × width ^{2} × 0.5) was calculated and measured until the tumor reached the ethically allowed maximum volume of 2,000 mm^3 or the health of the mice was seriously deteriorated (censored events).

Patient-derived CRC xenografts zebrafish models

For the PDX zebrafish model, Tg (flk1:EGFP) transgenic zebrafish embryos at 48 hr were selected, and 400 tumor cells per embryo were microinjected to establish a zebrafish transplantation model of the tumor cell line. After transplantation, the embryos were placed in an incubator at 34 °C with lighting for 24 hours (14 hours of light, 10 hours of dark). After 24 hours, embryos with a consistent number of transplanted tumor cells were randomly divided into four groups for treatment with DMSO, palbociclib (0.5 μM), erlotinib (1 μM), and their combination. After treatment, they were returned to the 37 °C light incubator for cultivation. After 72 hours, confocal imaging was performed

and proliferation was calculated using GraphPad Prism software.

Bioinformatic analysis

The BGI Genomics sequencing analysis platform, Dr. Tom（https://biosys.bgi.com) is used for KEGG, GO, and GSEA. The BioLadder (https://www.bioladder.cn/web/#/pro/cloud) online plotting software is used to create volcano plots. The online STRING (https://cn.string-db.org/) protein interaction website is utilized for the analysis of EGFR interacting proteins. We used Rstudio for heatmap generation (Pretty Heatmaps, Ggplot2). The (GSEA) http://software.broadinstitute.org/gsea/msigdb/ index.jsp) software programs were used to analyze the high-throughput data.

Statistical analysis

The *in vitro* data in the figures are represented as the mean ± SD and the data of PDX tumor growth are presented as mean ±SEM (standard error of the mean). Statistical significance was calculated by Student's t-test or ANOVA using GraphPad Prism. The *in vitro* experiments were performed in triplicate and replicated in more than two independent experiments. The statistical significance of differences is indicated in figures by asterisks as follows: *, P <0.05; **, P <0.01; ***, P <0.001.

LEGENDS

Figure 1. Palbociclib antitumor activity and PIK3CA mutations promote palbociclib resistance in colorectal cancer.

A, Growth inhibition curves and IC50 values for five CRC cell lines treated with palbociclib. **B,** Images showing the colony formation of five CRC cell lines after palbociclib treatment. **C,** Table of PIK3CA gene mutations in five CRC cell lines from the CCLE database. **D,** Immunoblot for RB, p-RB and FoxM1 from five CRC cell lines with palbociclib treatment. **E,** Analysis of the mutational profiles of palbociclib-resistant (IC50 > 10 μM) and sensitive (IC50 < 10 μM) cells from the GDASC database. **F,** Mutational landscape of CRC from TCGA data and PIK3CA gene mutations (E545K/G and H1047R/L) from the GSCA database. **G,** Tumor volume curves of CDX models (LOVO-PIK3CA WT and MUT cells) after vehicle or palbociclib treatment. **H,** Kaplan-Meier curves depicting OS for CDX mice (LOVO-PIK3CA WT and MUT cells) treated with vehicle or palbociclib. **I,** Representative

images of CDX mice (LOVO-PIK3CA WT and MUT cells) after vehicle or palbociclib treatment. Mean ± SD; Mean ± SEM; *, $P < 0.05$, **, $P < 0.01$; and ***, $P < 0.001$.

Figure 2. PIK3CA mutations enhance palbociclib-induced senescence and alter SASP gene expression.

A, Schematic of RNA-sequencing on LOVO-PIK3CA WT and MUT cell lines treated with palbociclib. KEGG analysis of RNA-sequencing datas from LOVO-PIK3CA WT (**B**) and MUT (**C**) cell lines with palbociclib treatment. **D,** β-galactosidase staining of LOVO-PIK3CA WT and MUT cell lines treated with palbociclib (Scale bar: 20 μm). **E,** Quantitation of the percentage of β-galactosidase-positive cells (by image **D**). **F,** Immunoblot for p-RB, p21, pAKT-308 from LOVO-PIK3CA WT and MUT cell lines with palbociclib treatment. **G,** Immunoblot analysis of Senescence marker proteins in LOVO-PIK3CA WT and MUT cell lines. **H,** Immunoblot of G1 phase regulatory proteins from LOVO-PIK3CA WT and MUT cell lines. **I,** GSEA enrichment analysis of RNA-sequencing data from LOVO-PIK3CA WT and MUT cell lines with palbociclib treatment. **J,** Venn diagram (right) depicting overlap between SASP genes in palbociclib-treated LOVO-PIK3CA WT and MUT cell lines. Heatmap (left) depicting the expression of 240 common SASP genes. **K,** Volcano plot of SASP genes expression from RNA-sequencing datas. **I,** mRNA expression of SASP genes from LOVO-PIK3CA WT and MUT cell lines treated with palbociclib. Mean ± SD; *, $P < 0.05$, **, $P < 0.01$; and ***, $P < 0.001$.

Figure 3. SASP factors in palbociclib-induced PIK3CA mutant cell lines lead to resistance by upregulating EGFR.

A, Schematic illustrating the experimental approach of treating LOVO-PIK3CA WT and MUT cell lines with palbociclib, then collecting senescent conditioned medium (S-CM) for further experiments. **B,** Short-term proliferation assays of LOVO-PIK3CA WT and MUT cell lines upon treatment S-CM and control. **C,** Images showing the colony formation of LOVO-PIK3CA WT and MUT cell lines upon treatment S-CM and control. **D,** Growth inhibition curves and IC50 values of LOVO-PIK3CA WT and MUT cell lines exposed to S-CM and control under palbociclib treatment. **E,** GSEA enrichment analysis of RNA-sequencing datas from LOVO-PIK3CA MUT cell lines with S-CM treatment. **F,** Immunoblot for EGFR pathway protein expression in LOVO-PIK3CA WT and MUT cell lines under S-CM time (0, 12, 24, 48, and 72 hours) and concentration (S-CM S-CM/DMEM = 1:1, 2:1, and 3:1)

gradient treatment. **G,** Immunoblot for EGFR expression in LOVO-PIK3CA WT and MUT cell lines. **I,** Growth inhibition curves and IC50 values for LOVO and SW620 cells overexpressing EGFR under palbociclib treatment. **H,** Immunoblot for EGFR expression in LOVO and SW620 cells overexpressing EGFR gene. **J,** Images showing the colony formation of LOVO and SW620 cells after overexpression of EGFR genes with palbociclib treatment. Mean ± SD; *, $P < 0.05$, **, $P < 0.01$; and ***, $P < 0.001$.

Figure 4. The SASP factor LCN2 enhances the expression of EGFR by suppressing ubiquitination and lysosomal degradation pathways.

A, The heatmap shows the expression of 69 key SASP genes in PIK3CA mutant cell lines. **B,** mRNA expression of LCN2 genes from LOVO-PIK3CA WT and MUT cell lines treated with palbociclib. **C,** ELISA to measure the secretion of LCN2 protein (ng/mL) in LOVO-PIK3CA WT and MUT cell lines treated with palbociclib. **D-E,** Immunoblot for EGFR expression in LOVO and SW620 cells after overexpression of LCN2 gene. **F-G,** mRNA expression of EGFR genes in LOVO and SW620 cells after overexpression of LCN2 gene. **H-I,** Images showing the colony formation of LOVO and SW620 cells after overexpression of LCN2 gene. **J,** Immunofluorescence images of EGFR (red) and LCN2 (green) LOVO and SW620 cells after overexpression of EGFR and LCN2 genes (Scale bar: 20 μm). **K,** Plot profile analysis of colocalization between EGFR and LCN2 proteins. **L,** Co-IP immunoblot of EGFR-Flag and LCN2-Flag in transfected HEK293T cells. **M-N,** Immunoblot for EGFR expression with treatment CHX (100 mg/mL) in LOVO and SW620 cell lines after overexpression of LCN2 gene and control. **O,** Immunoblot for EGFR expression with treatment CHX (100 mg/mL) and MG132 in LOVO cell lines after overexpression of LCN2 gene and control. **P,** Immunoblot for EGFR expression with treatment CHX (100 mg/mL) and Leu in LOVO cell lines after overexpression of LCN2 gene and control. **Q,** Immunoblot analysis of changes in EGFR ubiquitination under overexpression of EGFR, HA-Ub and LCN2 genes. **R,** mRNA expression of TGFA genes from LOVO-PIK3CA WT and MUT cell lines treated with palbociclib. **S,** ELISA to measure the secretion of TGF-α protein (pg/mL) in LOVO-PIK3CA WT and MUT cell lines treated with palbociclib. **T,** Immunoblot for EGFR expression in the cell membrane and cytoplasm of LOVO and SW620 cells after overexpression of LCN2. ATP1A2 protein was used as a membrane protein positive control. Mean ± SD; *, $P < 0.05$, **, $P < 0.01$; and ***, $P < 0.001$.

Figure 5. The screening of a drug library for the combination of erlotinib and palbociclib reveals a significant synergistic anti-tumor effect.

A, Schematic diagram of drug library screening. **B,** Synergy index calculation for 133 tumor-targeting drugs with palbociclib. **C,** HSA synergy matrices showing the interaction between palbociclib and erlotinib in DLD1 and HCT15 cell lines (HSA > 0 indicate synergistic effects). **D,** CI plots showing the sturdy synergistic effect of palbociclib and erlotinib in DLD1 and HCT15 cell lines (CI < 1 indicates a synergistic effects). **E,** Growth inhibition curves of DLD1 and HCT15 cell lines treated with fixed concentration-combinations of palbociclib and erlotinib. **F,** Images showing the colony formation of DLD1 and HCT15 cell lines treated with palbociclib and/or erlotinib. **G,** Immunoblot for EGFR and p-RB downstream protein expression in DLD1 and HCT15 cells following treatment with palbociclib (20 nM), erlotinib (2 μM), or their combination. **H,** KEGG analysis of RNA-seq data comparing palbociclib + erlotinib to palbociclib in LOVO-PIK3CA MUT cells. **I,** Heatmap depicting the expression of 84 cell cycle genes following PE treatment. **J,** Cell cycle analysis of DLD1 and HCT15 cell lines upon treatment with palbociclib or erlotinib alone or in combination. **K,** The quantification of cell fractions in G1, S and G2/M phases in **J**. **L,** Apoptosis analysis of DLD1 and HCT15 cell lines upon treatment of palbociclib and/or erlotinib. Quantification of apoptotic cells in (**M**) by image (**L**). Mean ± SD; *, $P < 0.05$, **, $P < 0.01$; and ***, $P < 0.001$.

Figure 6. PE-combination exhibited significant efficacy in PDX models with PIK3CA mutation.

A, Images showing PDX cells with the PIK3CA H1047L mutation treated with palbociclib, erlotinib, or both in zebrafish. Quantification from image (**A**) is shown in **B**. **C,** Tumor volume curves of PDX (616#) after palbociclib and/or erlotinib treatment. **D,** Kaplan-Meier curves depicting OS for PDX (616#) mice treated with palbociclib and/or erlotinib. **E,** PDX (616#) tumor tissue from mice treated with palbociclib and/or erlotinib, stained for β-Gal, LCN2, and EGFR (Scale bars: 200 μm, 50 μm). Quantification from image (**E**) is shown in **F**. **G,** Representative images of PDX (616#) mice upon treatment of palbociclib and/or erlotinib. **H,** Images showing immunofluorescent staining of PDX (616#) tissues for LCN2 (green) and EGFR (red) proteins after treatment with palbociclib and/or erlotinib (scale bar: 50 μm). **I,** Representative images of PDX (44#) mice upon treatment of palbociclib and/or erlotinib. **J,** Tumor volume curves of PDX (44#) after palbociclib and/or erlotinib treatment. **K,** Kaplan-Meier curves depicting OS for PDX (44#) mice treated with palbociclib and/or erlotinib. Mean

± SD; Mean ± SEM; *, $P < 0.05$, **, $P < 0.01$; and ***, $P < 0.001$.

Figure 7. Diagram illustrating the research mechanism.

The study's mechanistic diagram shows that PIK3CA mutations alter the senescence phenotype and SASP gene expression induced by palbociclib, leading to increased EGFR protein expression and enhanced colorectal cancer resistance to the drug. The SASP factor LCN2 is key in upregulating EGFR by inhibiting its ubiquitination and reducing lysosomal degradation. Therapeutically, combining erlotinib with palbociclib could be beneficial.

Fig. 1

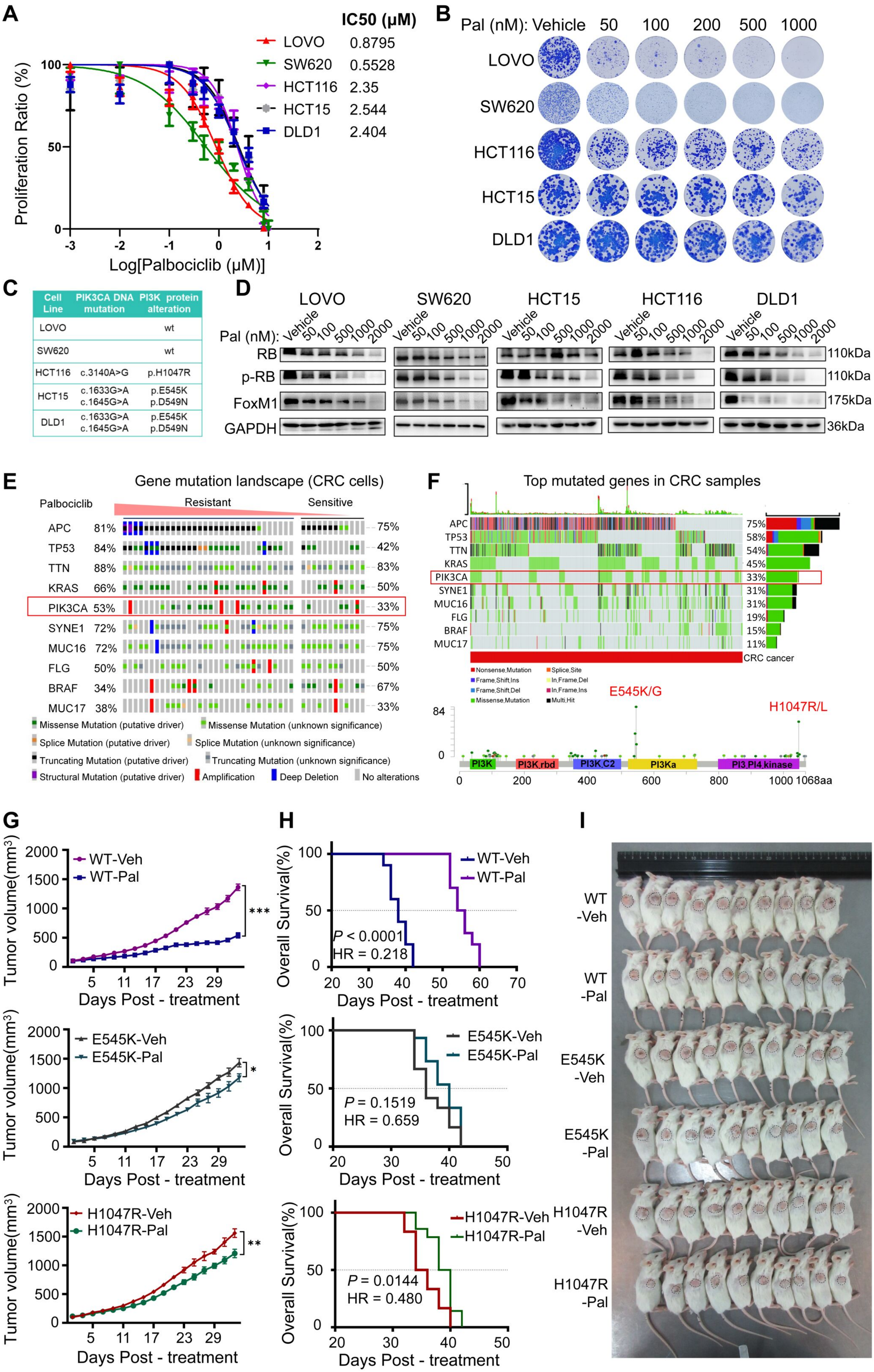
A
IC50 (μM)
LOVO 0.8795
SW620 0.5528
HCT116 2.35
HCT15 2.544
DLD1 2.404
Proliferation Ratio (%)
Log[Palbociclib (μM)]
B
Pal (nM): Vehicle 50 100 200 500 1000
LOVO
SW620
HCT116
HCT15
DLD1
C
Cell Line | PIK3CA DNA mutation | PI3K protein alteration
LOVO | wt
SW620 | wt
HCT116 | c.3140A>G | p.H1047R
HCT15 | c.1633G>A c.1645G>A | p.E545K p.D549N
DLD1 | c.1633G>A c.1645G>A | p.E545K p.D549N
D
LOVO SW620 HCT15 HCT116 DLD1
Pal (nM): Vehicle 50 100 500 1000 2000
RB 110kDa
p-RB 110kDa
FoxM1 175kDa
GAPDH 36kDa
E
Gene mutation landscape (CRC cells)
Palbociclib
Resistant
Sensitive
APC 81% 75%
TP53 84% 42%
TTN 88% 83%
KRAS 66% 50%
PIK3CA 53% 33%
SYNE1 72% 75%
MUC16 72% 75%
FLG 50% 50%
BRAF 34% 67%
MUC17 38% 33%
Missense Mutation (putative driver)
Missense Mutation (unknown significance)
Splice Mutation (putative driver)
Splice Mutation (unknown significance)
Truncating Mutation (putative driver)
Truncating Mutation (unknown significance)
Structural Mutation (putative driver)
Amplification
Deep Deletion
No alterations
F
Top mutated genes in CRC samples
APC 75%
TP53 58%
TTN 54%
KRAS 45%
PIK3CA 33%
SYNE1 31%
MUC16 31%
FLG 19%
BRAF 15%
MUC17 11%
CRC cancer
Nonsense_Mutation
Splice_Site
Frame_Shift_Ins
In_Frame_Del
Frame_Shift_Del
In_Frame_Ins
Missense_Mutation
Multi_Hit
E545K/G
H1047R/L
PI3K
PI3K_rbd
PI3K_C2
PI3Ka
PI3_PI4_kinase
1068aa
G
Tumor volume(mm³)
WT-Veh
WT-Pal
E545K-Veh
E545K-Pal
H1047R-Veh
H1047R-Pal
Days Post - treatment
H
Overall Survival(%)
P < 0.0001
HR = 0.218
P = 0.1519
HR = 0.659
P = 0.0144
HR = 0.480
I
WT -Veh
WT -Pal
E545K -Veh
E545K -Pal
H1047R -Veh
H1047R -Pal

Fig. 2

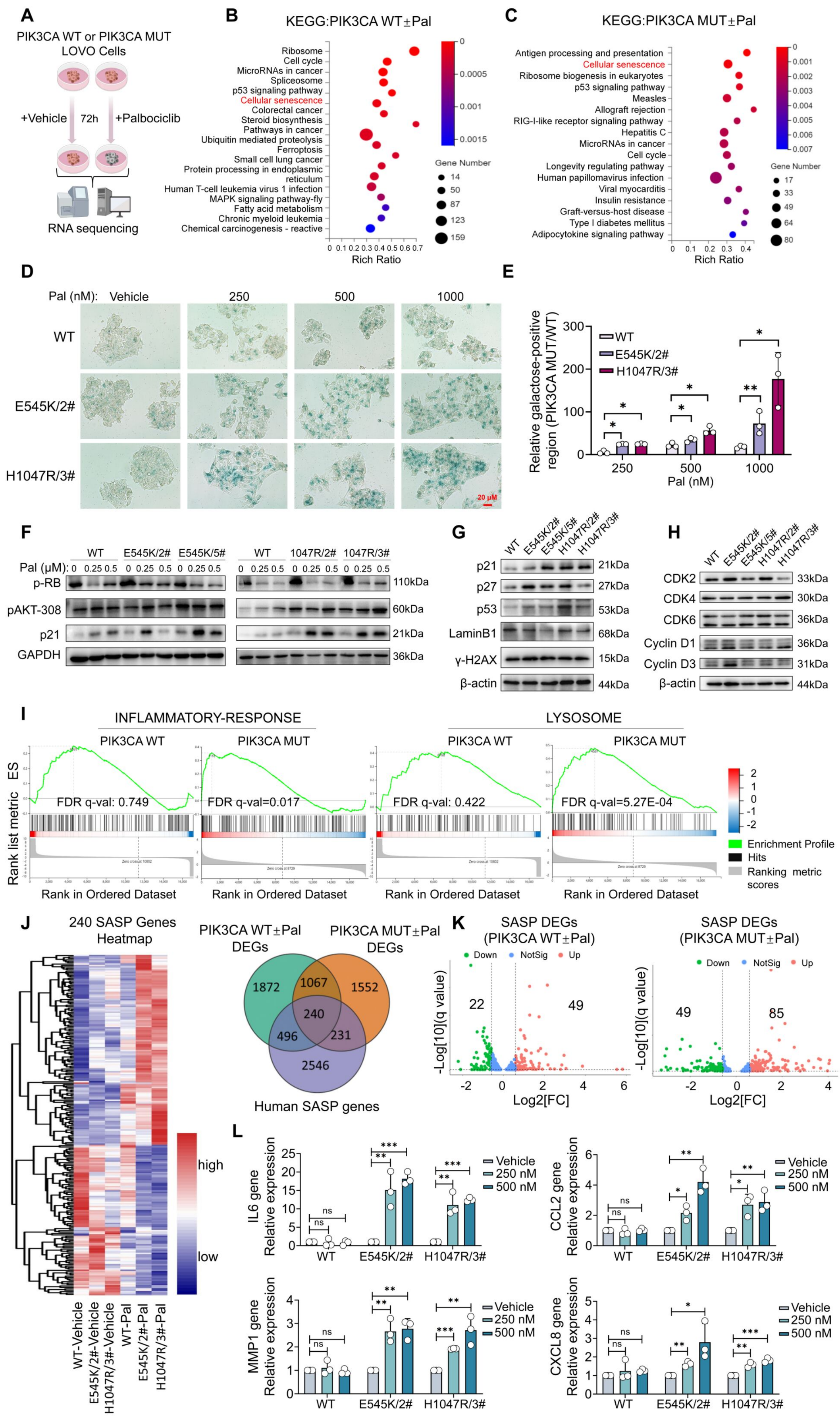
A
PIK3CA WT or PIK3CA MUT LOVO Cells
+Vehicle
72h
+Palbociclib
RNA sequencing
B
KEGG:PIK3CA WT±Pal
Ribosome
Cell cycle
MicroRNAs in cancer
Spliceosome
p53 signaling pathway
Cellular senescence
Colorectal cancer
Steroid biosynthesis
Pathways in cancer
Ubiquitin mediated proteolysis
Ferroptosis
Small cell lung cancer
Protein processing in endoplasmic reticulum
Human T-cell leukemia virus 1 infection
MAPK signaling pathway-fly
Fatty acid metabolism
Chronic myeloid leukemia
Chemical carcinogenesis - reactive
Rich Ratio
Gene Number
C
KEGG:PIK3CA MUT±Pal
Antigen processing and presentation
Cellular senescence
Ribosome biogenesis in eukaryotes
p53 signaling pathway
Measles
Allograft rejection
RIG-I-like receptor signaling pathway
Hepatitis C
MicroRNAs in cancer
Cell cycle
Longevity regulating pathway
Human papillomavirus infection
Viral myocarditis
Insulin resistance
Graft-versus-host disease
Type I diabetes mellitus
Adipocytokine signaling pathway
Rich Ratio
Gene Number
D
Pal (nM): Vehicle 250 500 1000
WT
E545K/2#
H1047R/3#
20 μM
E
Relative galactose-positive region (PIK3CA MUT/WT)
WT
E545K/2#
H1047R/3#
Pal (nM)
F
WT E545K/2# E545K/5# WT 1047R/2# 1047R/3#
Pal (μM): 0 0.25 0.5 0 0.25 0.5 0 0.25 0.5 0 0.25 0.5 0 0.25 0.5 0 0.25 0.5
p-RB
pAKT-308
p21
GAPDH
110kDa
60kDa
21kDa
36kDa
G
WT E545K/2# E545K/5# H1047R/2# H1047R/3#
p21 21kDa
p27 27kDa
p53 53kDa
LaminB1 68kDa
γ-H2AX 15kDa
β-actin 44kDa
H
WT E545K/2# E545K/5# H1047R/2# H1047R/3#
CDK2 33kDa
CDK4 30kDa
CDK6 36kDa
Cyclin D1 36kDa
Cyclin D3 31kDa
β-actin 44kDa
I
INFLAMMATORY-RESPONSE
LYSOSOME
PIK3CA WT
PIK3CA MUT
FDR q-val: 0.749
FDR q-val=0.017
FDR q-val: 0.422
FDR q-val=5.27E-04
ES
Rank list metric
Rank in Ordered Dataset
Enrichment Profile
Hits
Ranking metric scores
J
240 SASP Genes Heatmap
PIK3CA WT±Pal DEGs
PIK3CA MUT±Pal DEGs
1872
1067
1552
240
496
231
2546
Human SASP genes
high
low
WT-Vehicle
E545K/2#-Vehicle
H1047R/3#-Vehicle
WT-Pal
E545K/2#-Pal
H1047R/3#-Pal
K
SASP DEGs (PIK3CA WT±Pal)
SASP DEGs (PIK3CA MUT±Pal)
Down
NotSig
Up
22
49
49
85
-Log[10](q value)
Log2[FC]
L
IL6 gene Relative expression
CCL2 gene Relative expression
MMP1 gene Relative expression
CXCL8 gene Relative expression
Vehicle
250 nM
500 nM
WT
E545K/2#
H1047R/3#

Fig. 3

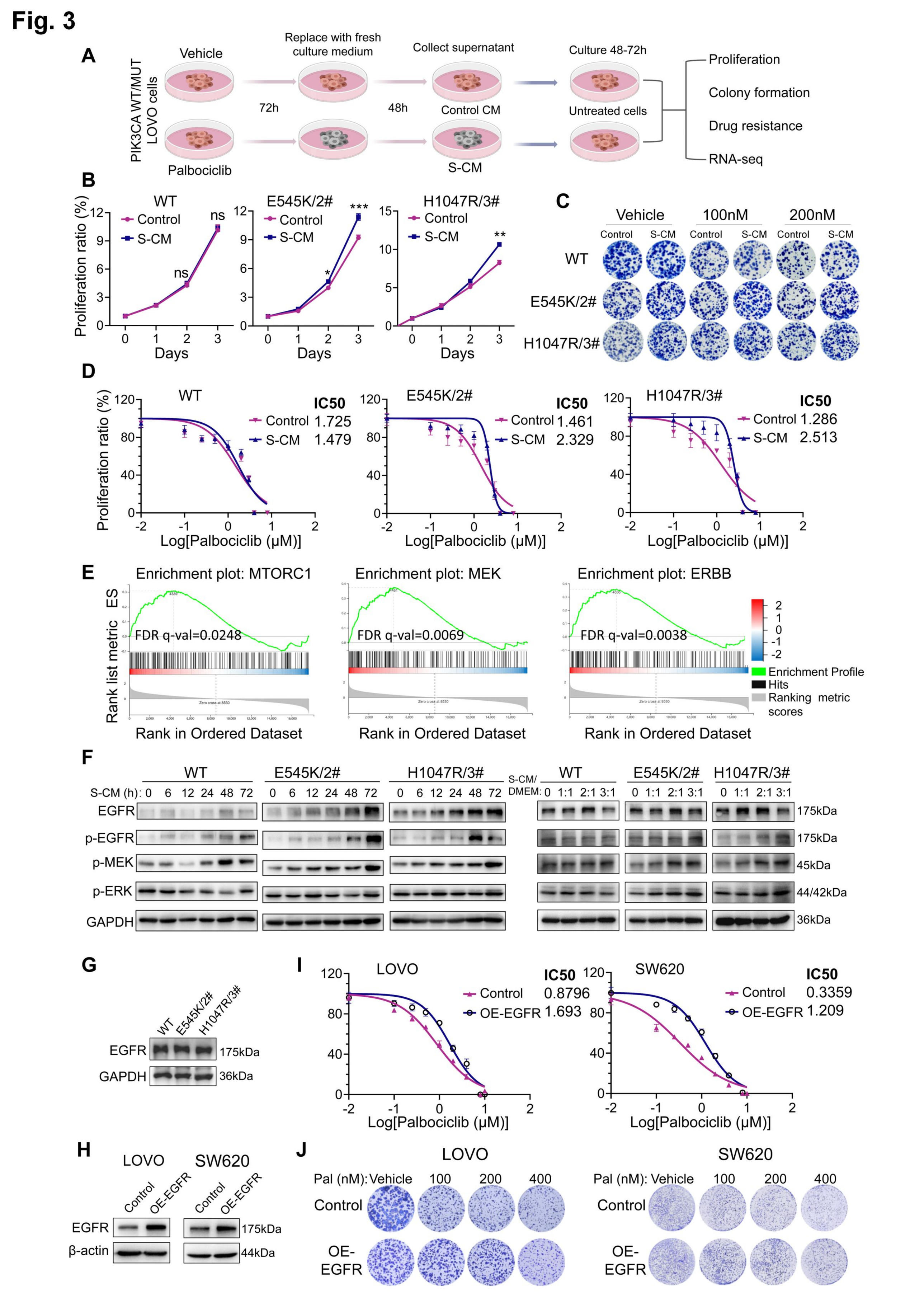
A
PIK3CA WT/MUT LOVO cells
Vehicle
Palbociclib
72h
Replace with fresh culture medium
48h
Collect supernatant
Control CM
S-CM
Culture 48-72h
Untreated cells
Proliferation
Colony formation
Drug resistance
RNA-seq
B
WT
E545K/2#
H1047R/3#
Control
S-CM
Proliferation ratio (%)
Days
ns
*
***
**
C
Vehicle
100nM
200nM
Control
S-CM
WT
E545K/2#
H1047R/3#
D
IC50
Control 1.725
S-CM 1.479
Control 1.461
S-CM 2.329
Control 1.286
S-CM 2.513
Log[Palbociclib (μM)]
E
Enrichment plot: MTORC1
Enrichment plot: MEK
Enrichment plot: ERBB
FDR q-val=0.0248
FDR q-val=0.0069
FDR q-val=0.0038
Rank list metric
ES
Rank in Ordered Dataset
Enrichment Profile
Hits
Ranking metric scores
F
S-CM (h): 0 6 12 24 48 72
S-CM/DMEM: 0 1:1 2:1 3:1
EGFR
p-EGFR
p-MEK
p-ERK
GAPDH
175kDa
45kDa
44/42kDa
36kDa
G
WT
E545K/2#
H1047R/3#
I
LOVO
SW620
Control
OE-EGFR
IC50
0.8796
1.693
0.3359
1.209
Log[Palbociclib (μM)]
H
β-actin
44kDa
J
Pal (nM): Vehicle 100 200 400

Fig. 4

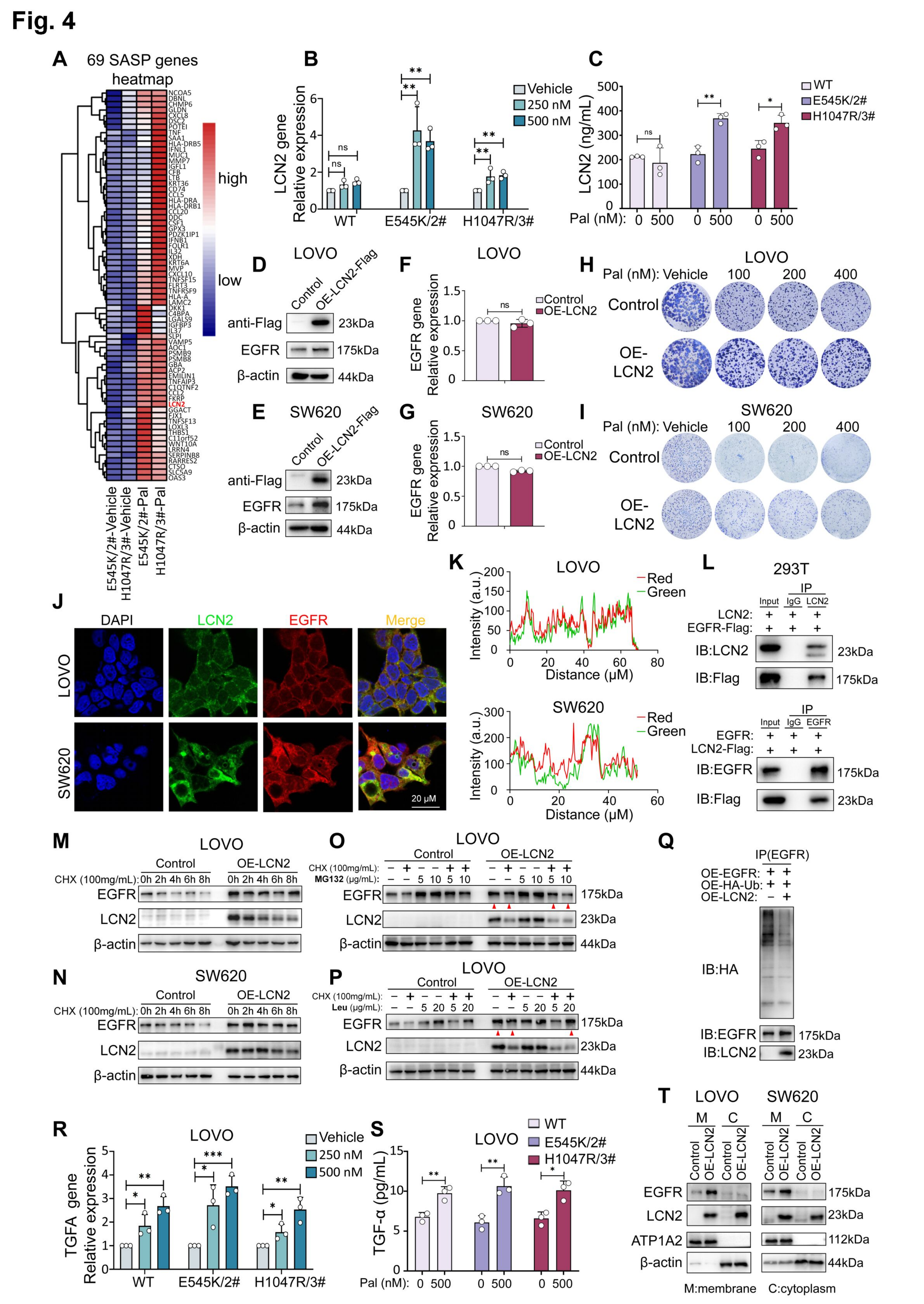
A
69 SASP genes heatmap
high
low
E545K/2#-Vehicle
H1047R/3#-Vehicle
E545K/2#-Pal
H1047R/3#-Pal
B
LCN2 gene Relative expression
Vehicle
250 nM
500 nM
WT
E545K/2#
H1047R/3#
C
LCN2 (ng/mL)
WT
E545K/2#
H1047R/3#
Pal (nM): 0 500 0 500 0 500
D
LOVO
Control
OE-LCN2-Flag
anti-Flag
23kDa
EGFR
175kDa
β-actin
44kDa
E
SW620
F
LOVO
EGFR gene Relative expression
Control
OE-LCN2
G
SW620
H
LOVO
Pal (nM): Vehicle 100 200 400
Control
OE-LCN2
I
SW620
J
DAPI
LCN2
EGFR
Merge
LOVO
SW620
20 μM
K
LOVO
Red
Green
Intensity (a.u.)
Distance (μM)
SW620
L
293T
IP
Input
IgG
LCN2
EGFR-Flag:
IB:LCN2
IB:Flag
EGFR
LCN2-Flag:
IB:EGFR
M
LOVO
CHX (100mg/mL): 0h 2h 4h 6h 8h
N
SW620
O
MG132 (μg/mL):
P
Leu (μg/mL):
Q
IP(EGFR)
OE-EGFR:
OE-HA-Ub:
OE-LCN2:
IB:HA
R
TGFA gene Relative expression
S
TGF-α (pg/mL)
T
M:membrane
C:cytoplasm
ATP1A2

Fig. 5

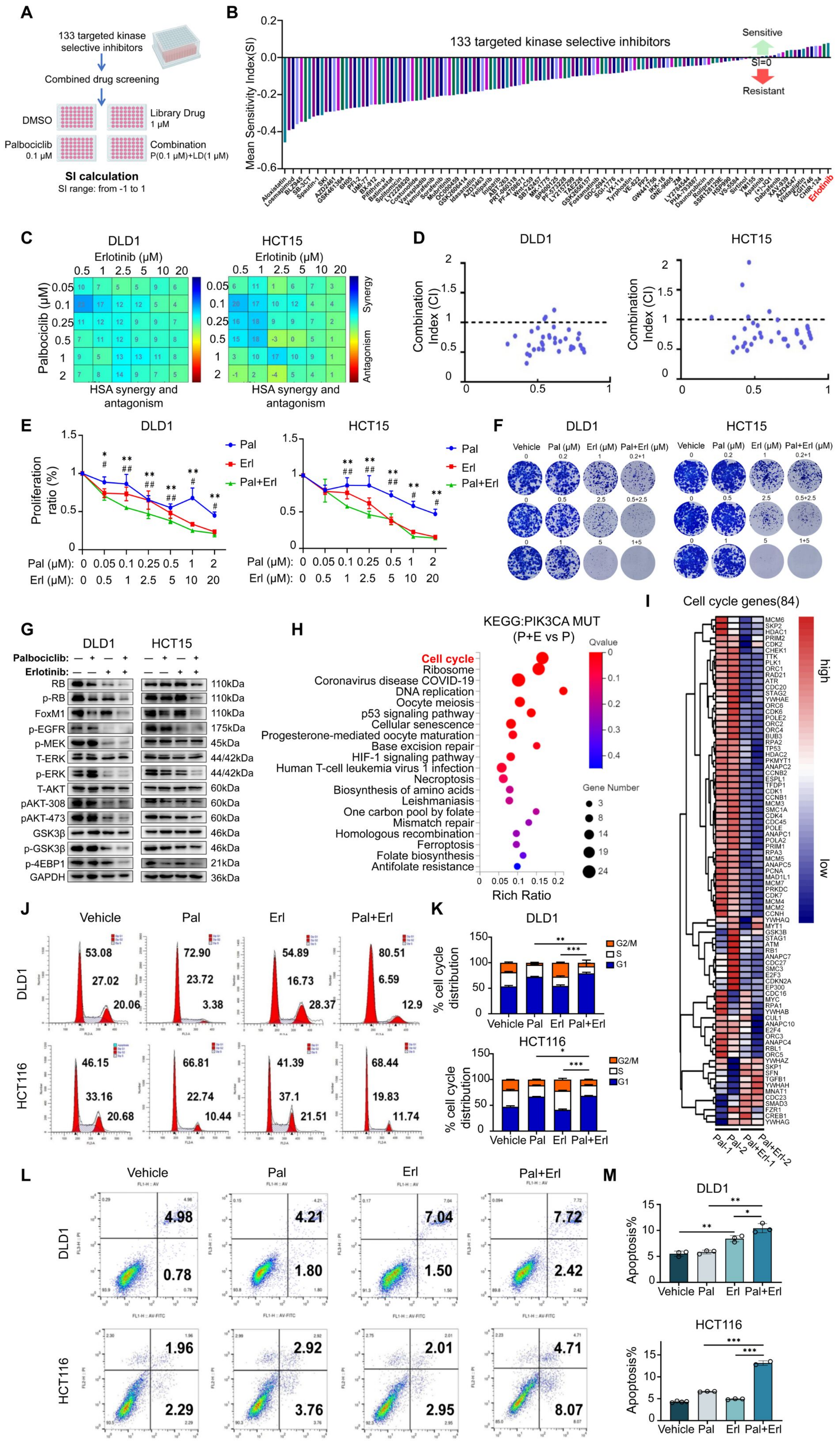
A
133 targeted kinase selective inhibitors
Combined drug screening
DMSO
Library Drug 1 μM
Palbociclib 0.1 μM
Combination P(0.1 μM)+LD(1 μM)
SI calculation
SI range: from -1 to 1
B
133 targeted kinase selective inhibitors
Mean Sensitivity Index(SI)
Sensitive
SI=0
Resistant
Erlotinib
C
DLD1
HCT15
Erlotinib (μM)
Palbociclib (μM)
Synergy
Antagonism
HSA synergy and antagonism
D
DLD1
HCT15
Combination Index (CI)
E
DLD1
HCT15
Proliferation ratio (%)
Pal
Erl
Pal+Erl
Pal (μM): 0 0.05 0.1 0.25 0.5 1 2
Erl (μM): 0 0.5 1 2.5 5 10 20
F
DLD1
HCT15
Vehicle
Pal (μM)
Erl (μM)
Pal+Erl (μM)
G
DLD1
HCT15
Palbociclib:
Erlotinib:
RB
p-RB
FoxM1
p-EGFR
p-MEK
T-ERK
p-ERK
T-AKT
pAKT-308
pAKT-473
GSK3β
p-GSK3β
p-4EBP1
GAPDH
110kDa
175kDa
45kDa
44/42kDa
60kDa
46kDa
21kDa
36kDa
H
KEGG:PIK3CA MUT (P+E vs P)
Cell cycle
Ribosome
Coronavirus disease COVID-19
DNA replication
Oocyte meiosis
p53 signaling pathway
Cellular senescence
Progesterone-mediated oocyte maturation
Base excision repair
HIF-1 signaling pathway
Human T-cell leukemia virus 1 infection
Necroptosis
Biosynthesis of amino acids
Leishmaniasis
One carbon pool by folate
Mismatch repair
Homologous recombination
Ferroptosis
Folate biosynthesis
Antifolate resistance
Qvalue
Gene Number
Rich Ratio
I
Cell cycle genes(84)
high
low
Pal-1
Pal-2
Pal+Erl-1
Pal+Erl-2
J
Vehicle
Pal
Erl
Pal+Erl
DLD1
HCT116
K
DLD1
HCT116
% cell cycle distribution
G2/M
S
G1
Vehicle Pal Erl Pal+Erl
L
Vehicle
Pal
Erl
Pal+Erl
DLD1
HCT116
M
DLD1
HCT116
Apoptosis%
Vehicle Pal Erl Pal+Erl

Fig. 6

616# PDX (PIK3CA H1047L)

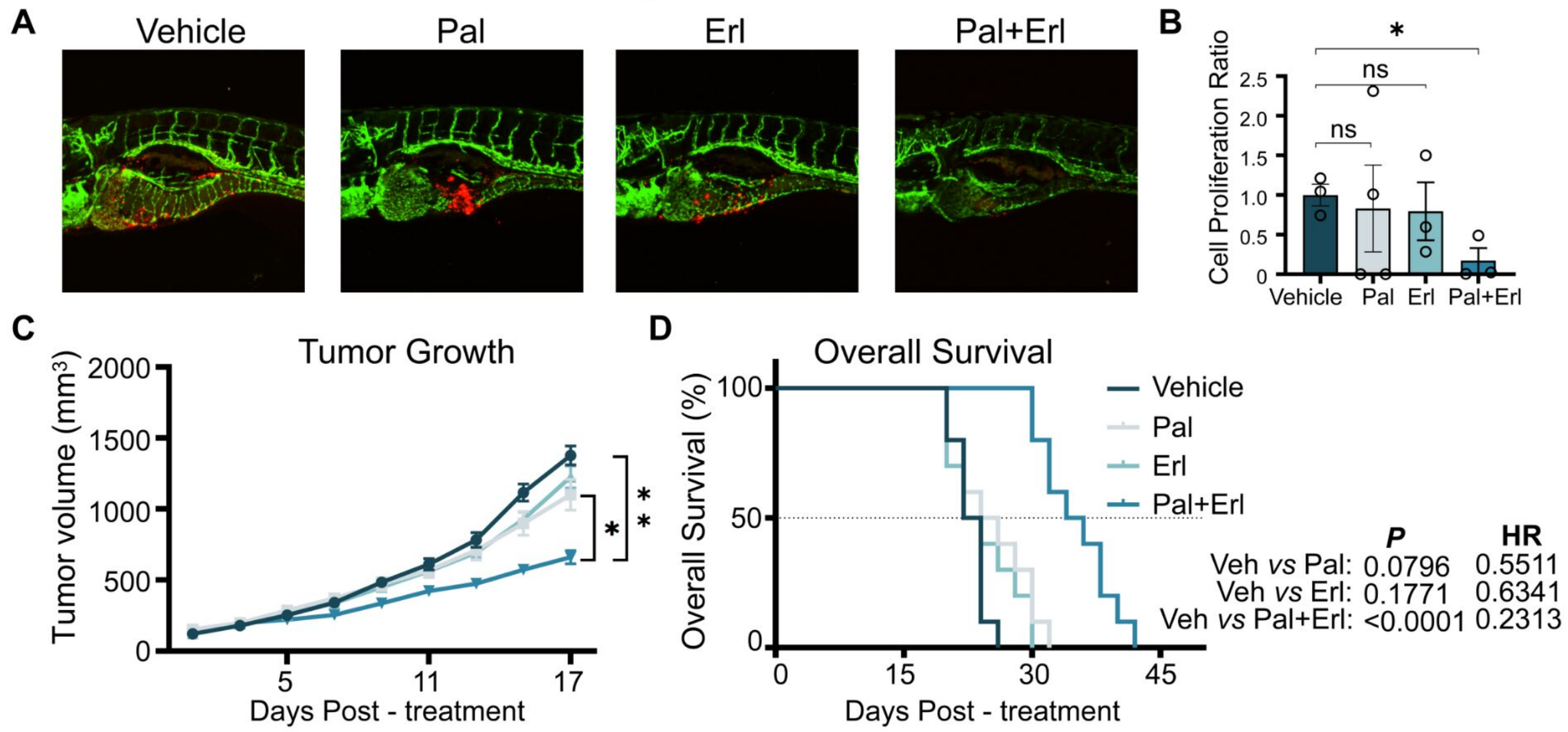

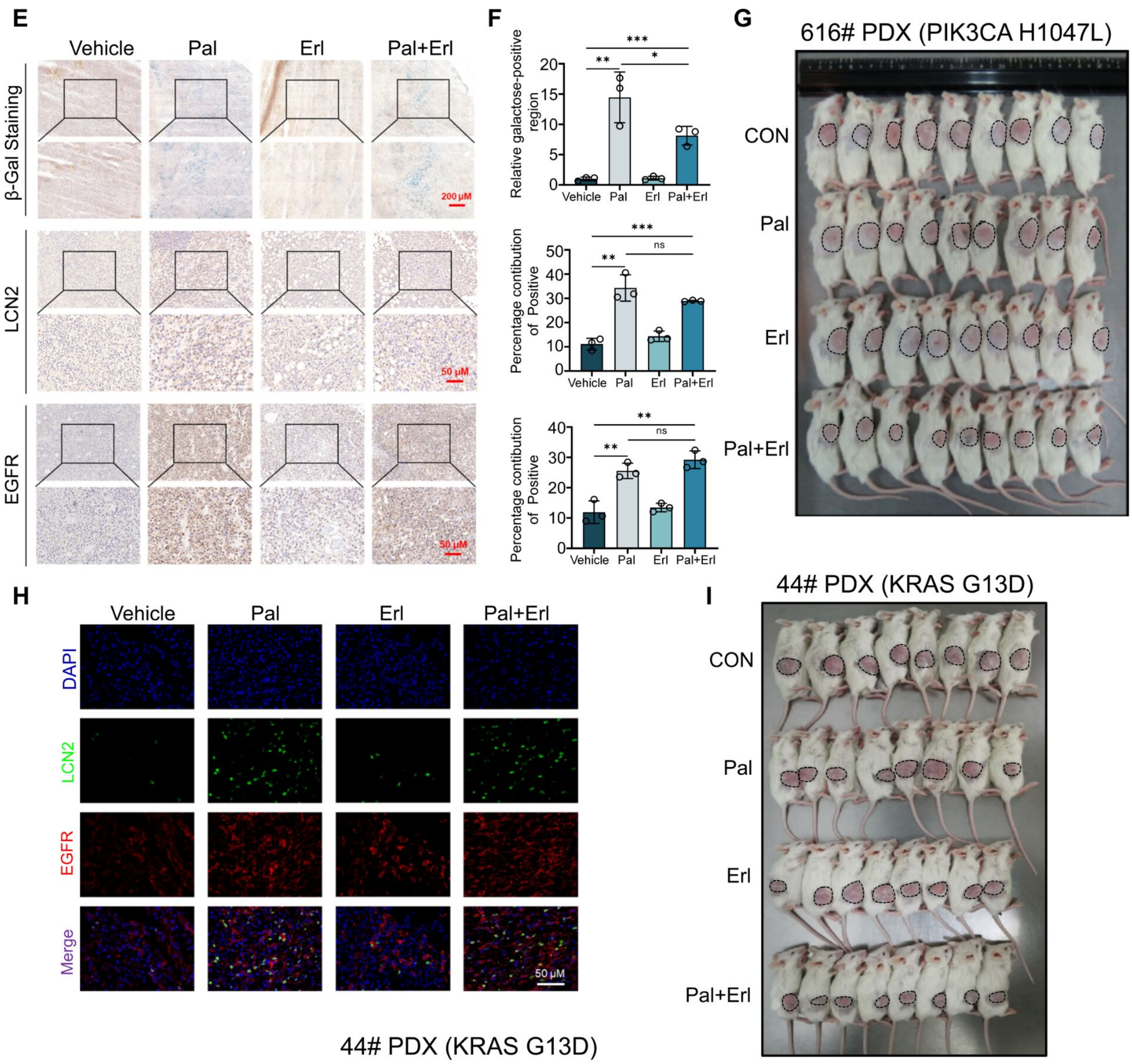

44# PDX (KRAS G13D)

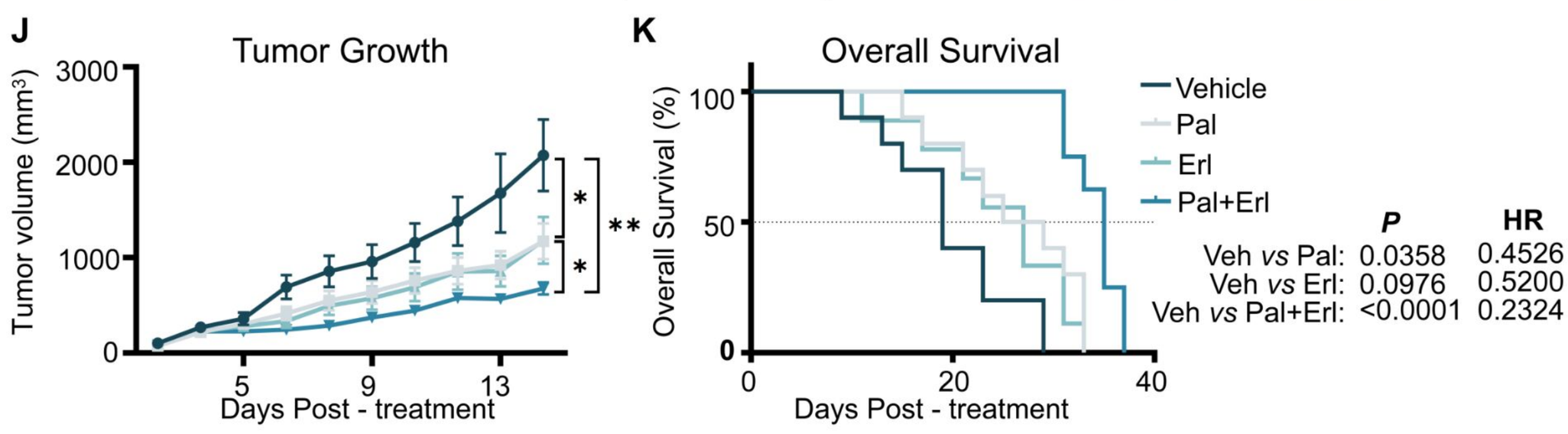

Fig. 7

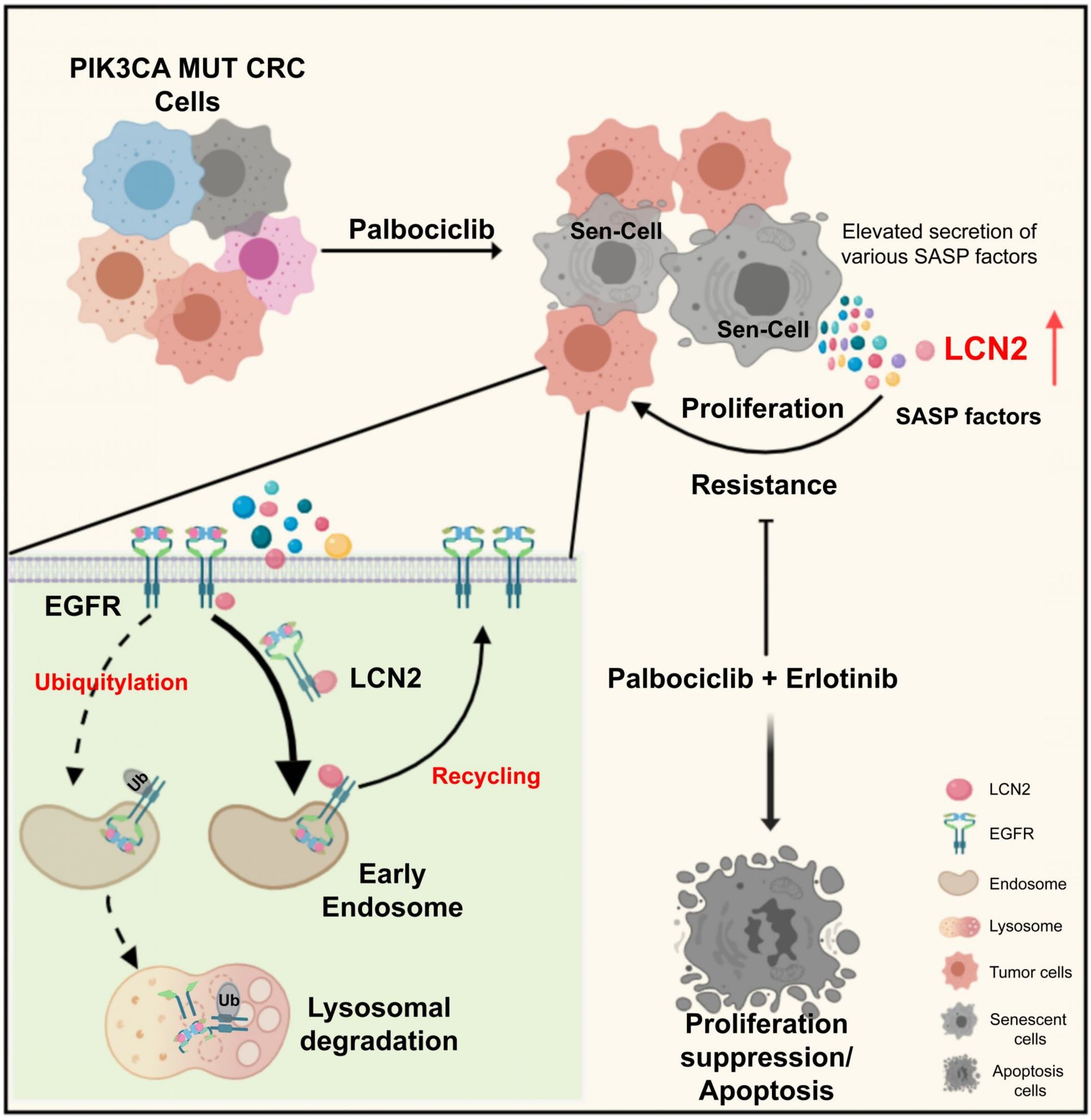
PIK3CA MUT CRC Cells
Palbociclib
Sen-Cell
Sen-Cell
Elevated secretion of various SASP factors
LCN2
Proliferation
SASP factors
Resistance
EGFR
Ubiquitylation
LCN2
Palbociclib + Erlotinib
Ub
Recycling
Early Endosome
Ub
Lysosomal degradation
Proliferation suppression/ Apoptosis
LCN2
EGFR
Endosome
Lysosome
Tumor cells
Senescent cells
Apoptosis cells